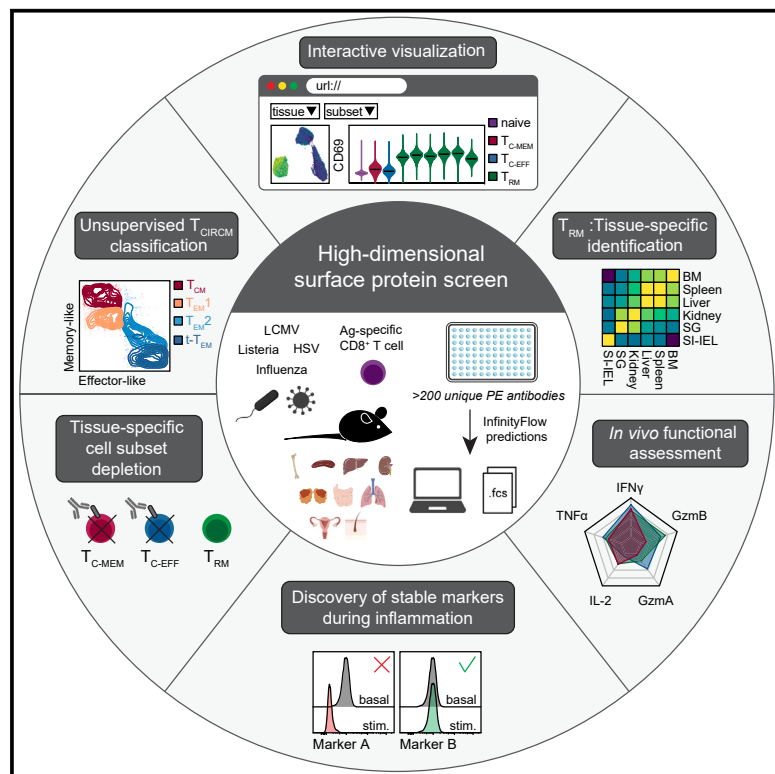


Immunity

Single-cell protein expression profiling resolves circulating and resident memory T cell diversity across tissues and infection contexts

Graphical abstract



Authors

Maximilien Evrard, Etienne Becht,
Raissa Fonseca, ..., Raphael Gottardo,
Evan W. Newell, Laura K. Mackay

Correspondence

maximilien.evrard@unimelb.edu.au
(M.E.),
lkmackay@unimelb.edu.au (L.K.M.)

In brief

Distinguishing between circulating (T_{CIRCM}) and tissue-resident memory T (T_{RM}) cells is challenging, particularly in tissues where they coexist. By profiling hundreds of surface proteins at the single-cell level, Evrard et al. reveal markers allowing the identification, targeted depletion, and functional characterization of T_{CIRCM} and T_{RM} populations across tissues and infection contexts.

Highlights

- InfinityFlow profiling of CD8⁺ T cells across tissues and infection models
- Resolution of T_{CIRCM} and T_{RM} cell-specific phenotypes across different organs
- Development of tissue-specific T_{CIRCM} or T_{RM} cell depletion strategies
- Discovery of stable markers for T_{CIRCM} and T_{RM} cell functional characterization



Resource

Single-cell protein expression profiling resolves circulating and resident memory T cell diversity across tissues and infection contexts

Maximilien Evrard,^{1,*} Etienne Becht,^{2,7} Raissa Fonseca,^{1,7} Andreas Obers,¹ Simone L. Park,¹ Nagela Ghabdan-Zanluqui,¹ Jan Schroeder,¹ Susan N. Christo,¹ Dominik Schienstock,¹ Junyun Lai,^{3,4} Thomas N. Burn,¹ Allison Clatch,¹ Imran G. House,^{3,4} Paul Beavis,^{3,4} Axel Kallies,¹ Florent Ginhoux,⁵ Scott N. Mueller,¹ Raphael Gottardo,^{2,6} Evan W. Newell,² and Laura K. Mackay^{1,8,*}

¹Department of Microbiology and Immunology, The University of Melbourne at The Peter Doherty Institute for Infection and Immunity, Parkville, VIC 3010, Australia

²Vaccine and Infectious Disease Division, Fred Hutchinson Cancer Research Center, Seattle, WA 98109, USA

³Sir Peter MacCallum Department of Oncology, The University of Melbourne, Parkville, VIC 3010, Australia

⁴Cancer Immunology Program, Peter MacCallum Cancer Centre, Parkville, VIC 3010, Australia

⁵Singapore Immunology Network (SIgN), Agency for Science, Technology and Research (A*STAR), Singapore 138648, Singapore

⁶Centre Hospitalier Universitaire du Vaud and University of Lausanne, Lausanne 1011, Switzerland

⁷These authors contributed equally

⁸Lead contact

*Correspondence: maximilien.evrard@unimelb.edu.au (M.E.), lkmacay@unimelb.edu.au (L.K.M.)

<https://doi.org/10.1016/j.immuni.2023.06.005>

SUMMARY

Memory CD8⁺ T cells can be broadly divided into circulating (T_{CIRCM}) and tissue-resident memory T (T_{RM}) populations. Despite well-defined migratory and transcriptional differences, the phenotypic and functional delineation of T_{CIRCM} and T_{RM} cells, particularly across tissues, remains elusive. Here, we utilized an antibody screening platform and machine learning prediction pipeline (InfinityFlow) to profile >200 proteins in T_{CIRCM} and T_{RM} cells in solid organs and barrier locations. High-dimensional analyses revealed unappreciated heterogeneity within T_{CIRCM} and T_{RM} cell lineages across nine different organs after either local or systemic murine infection models. Additionally, we demonstrated the relative effectiveness of strategies allowing for the selective ablation of T_{CIRCM} or T_{RM} populations across organs and identified CD55, KLRG1, CXCR6, and CD38 as stable markers for characterizing memory T cell function during inflammation. Together, these data and analytical framework provide an in-depth resource for memory T cell classification in both steady-state and inflammatory conditions.

INTRODUCTION

CD8⁺ memory T cells can be divided into two broad categories based on their migratory behavior, with circulating memory T (T_{CIRCM}) cells mainly found in the blood and lymphoid organs, and tissue-resident memory T (T_{RM}) cells dwelling in the periphery.^{1,2} T_{CIRCM} cells can be further divided into functionally distinct central memory T (T_{CM}) cells, effector memory T (T_{EM}) cells, and terminally differentiated T_{EM} (t- T_{EM}) cells.^{3–5} T_{CM} cells are characterized by CD62L and CCR7 expression that enables lymph node entry and exhibit enhanced antigen recall capacity and long-term persistence. In contrast, T_{EM} and t- T_{EM} cells display a comparatively shorter life span, with T_{EM} cells being the principal subset recirculating through non-lymphoid organs, while t- T_{EM} cells are mostly associated with the vasculature.^{6–8} In peripheral tissues such as the intestine, skin, and liver, immune surveillance is primarily mediated by T_{RM} cells that act as non-recirculating

sentinels providing long-lasting immune protection independently of T_{CIRCM} cells.^{1,2,9–11}

Despite major transcriptional and migratory differences,^{2,8,12} the delineation and targeted manipulation of T_{RM} and T_{CIRCM} cells remains challenging due to the lack of stable markers that can serve to identify and/or eliminate these populations. For instance, the release of ectoenzyme substrates during lymphocyte isolation from tissues can alter the expression of T cell surface molecules including CD27, CD62L, and P2RX7.^{13,14} Further, inflammatory stimuli and T cell receptor (TCR) signaling can modify the expression of lineage-defining markers such as the canonical T_{RM} cell marker CD69, preventing faithful classification of T_{RM} and T_{CIRCM} cell subsets in active immune environments.^{15,16} Finally, even though systemic antibody treatments have been used to eliminate T_{CIRCM} cells while sparing T_{RM} cells at physically segregated epithelial sites,^{17–19} approaches enabling the selective depletion of memory T cell subsets co-inhabiting tissues are still lacking.



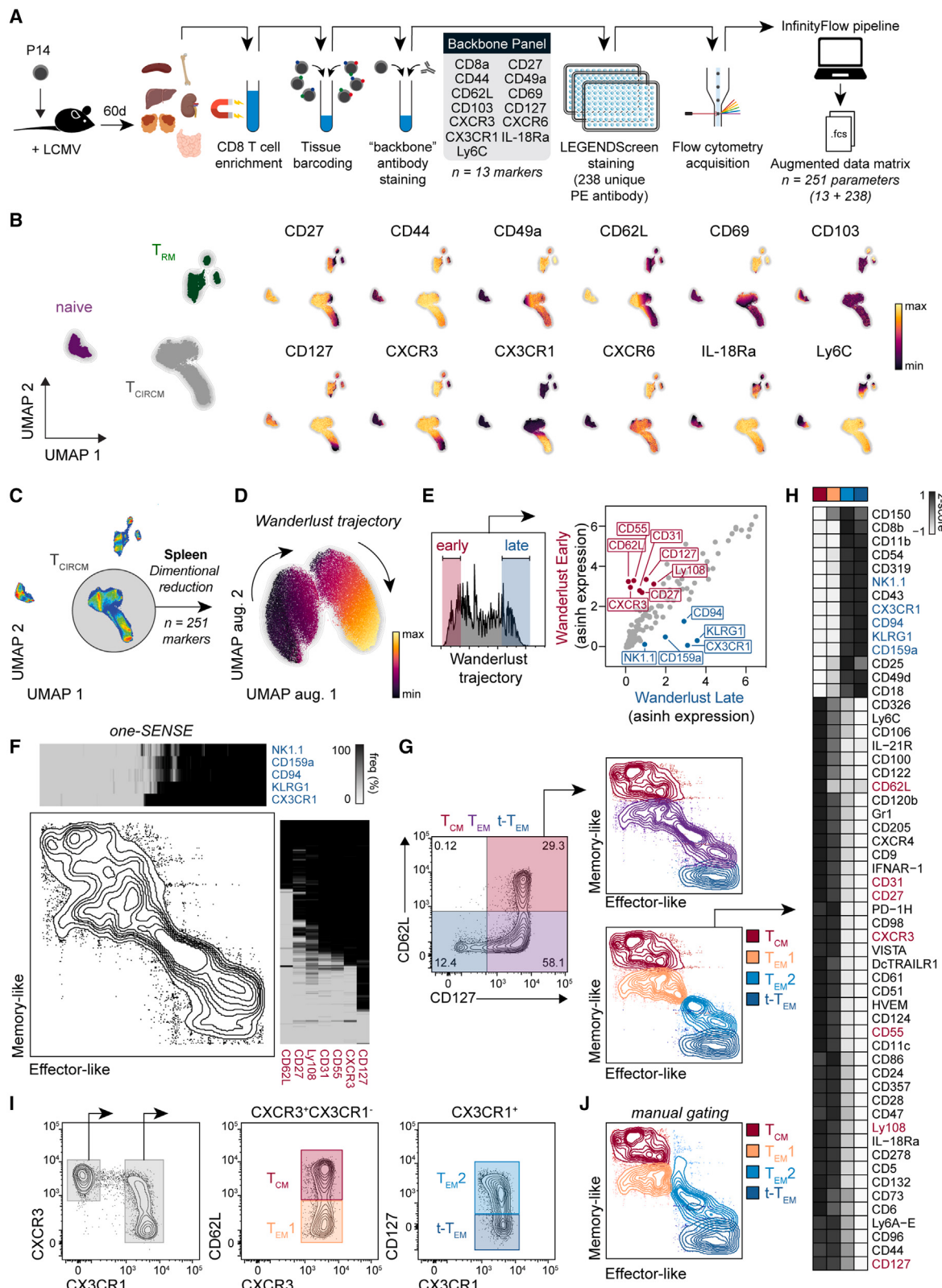


Figure 1. InfinityFlow unveils memory CD8⁺ T cell phenotypic diversity

(A) InfinityFlow analysis pipeline. Naive P14 Thy1.1⁺ T cells were primed using LCMV, isolated from various tissues 60 dpi, barcoded, and stained with a backbone antibody panel. Cells were stained with >200 PE-conjugated antibodies (LEGENDScreen), acquired by flow cytometry and analyzed using InfinityFlow.

(legend continued on next page)

To probe heterogeneity between T cell subsets, single-cell transcriptomic approaches are being increasingly applied.^{20–24} However, these methods can lack the sensitivity required to capture lowly expressed transcripts and may also identify differentially expressed genes that do not correlate with protein expression.²⁵ In contrast, surface proteins are often expressed at a higher magnitude than mRNA for the same gene,²⁶ allowing for reliable phenotypic tracking and cell purification strategies via flow cytometry. Here, to delineate surface phenotype variation between T_{CIRCM} and T_{RM} cell subsets, we employed InfinityFlow, a computational approach applying iterative protein measurements by flow cytometry to predict the expression of hundreds of markers at the single-cell level.^{27,28} We generated a surface protein map of CD8⁺ T cell differentiation states over nine different organs following infection, and extensively characterized memory T cell diversity within both circulating and resident compartments. From this, we revealed surface molecules allowing classification, targeted depletion, and the functional characterization of T_{CIRCM} and T_{RM} populations at steady-state and during acute inflammation, and moreover, identified CD38 as a regulator of T_{RM} cell development. This protein atlas resource enables the phenotypic interrogation of CD8⁺ T cells across tissues, infection models and time, via our interactive *Shiny* app (<http://mackaylab.mdhs.unimelb.edu.au/InfinityFlow/>), which will facilitate future studies to investigate memory T cell biology in health and disease.

RESULTS

Highly multiplexed characterization of the CD8⁺ T cell surface proteome across tissues using InfinityFlow

To interrogate memory CD8⁺ T cell heterogeneity across murine organs, we utilized lymphocytic choriomeningitis virus (LCMV-Armstrong), an acute infection model that generates T_{RM} cells in multiple tissue sites.^{15,29} To track CD8⁺ T cells, we transferred congenically marked LCMV GP_{33–41}-specific P14 T cells into wild-type (WT) recipients prior to infection. Mice were sacrificed >60 days post infection (dpi) and cells isolated from the spleen, bone marrow (BM), liver, kidney, salivary glands (SG), and small-intestine epithelium (SI-IEL). P14 T cells were barcoded according to tissue origin and stained with a “backbone” panel containing markers commonly used for memory T cell classification (Figures 1A and S1A–S1C; Tables S1 and S2). We then performed massively parallelized cytometry experiments using the LEGENDScreen platform that contains >200 distinct phycoerythrin (PE)-conjugated antibodies across individual wells and utilized the InfinityFlow machine learning pipeline to predict co-expression of

individually PE-tagged markers (Figures 1A, 1B, and S1C–S1E).²⁷ By combining data from each well with the information contained in the backbone panel, this method enabled data imputation into an augmented data matrix, allowing for the prediction of markers expressed by CD8⁺ T cells (Figures 1A, 1B, S1D, and S1E).

To evaluate InfinityFlow predictions, we performed uniform manifold approximation and projection (UMAP)³⁰ analysis using markers from the backbone panel and identified three main clusters corresponding to naive, T_{CIRCM} , and T_{RM} cells (Figure 1B). As anticipated, the comparison of predicted median intensities between clusters revealed that molecules not included in the backbone panel but typically associated with naive (CCR7), T_{CIRCM} (CD122, KLRG1), and T_{RM} (CD11a/LFA-1, CD279/PD-1) cells adhered to expected expression patterns across T cell subsets (Figure S1F). Furthermore, this method predicted expression of molecules in naive (Notch3, CD130), T_{CIRCM} (DR3, Ly6D), and T_{RM} (CD38, CD85k, CD160) cells whose function remains largely uncharacterized in these populations (Figures S1F and S1G).

Unsupervised characterization of T_{CIRCM} cells reveals extensive heterogeneity within the T_{EM} cell compartment

Circulating T cells comprise multiple subsets, with heterogeneity within the T_{EM} cell population being well appreciated.^{3,4,31,32} To provide an unbiased exploration of T_{CIRCM} cells, we performed UMAP analysis on the splenic T_{CIRCM} cluster using InfinityFlow predictions and employed trajectory inference³³ to order T_{CIRCM} cells along a pseudotime axis (Figure 1D). Comparison between “early” and “late” events as determined by pseudotime allowed for the identification of candidate markers stratifying T_{CIRCM} cells (Figure 1E). Early events showed co-expression of T cell memory-associated makers (e.g., CD62L, CD127, CXCR3), and expression of these molecules was progressively lost over the course of the trajectory, while markers associated with a terminally differentiated phenotype (e.g., CX3CR1, KLRG1) were enriched in late events (Figures S1H and S1I). We then used one-dimensional soli-expression by nonlinear stochastic embedding (one-SENSE) dimensionality reduction^{34,35} to assign individual markers to different categories of T_{CIRCM} cells. Assignment of T cells to “memory-like” or “effector-like” categories revealed two main subgroups of T_{CIRCM} cells (Figure 1F). To determine how these subgroups fit in the context of previously defined T_{CIRCM} populations,^{4,36,37} we overlaid T_{CM} , T_{EM} , and t- T_{EM} cells as defined by CD62L and CD127 onto the one-SENSE plot. While T_{CM} and t- T_{EM} cells were identified as the two most discordant states of this continuum, many T_{CIRCM} cells spanned a continuous range of differentiation

(B) (Left) UMAP plot of P14 T cell subsets generated using backbone markers, (right) colored by normalized expression of indicated markers.

(C and D) (C) UMAP dimensionality reduction and (D) Wanderlust trajectory analysis of T_{CIRCM} cells using InfinityFlow predictions, colored by pseudotime.

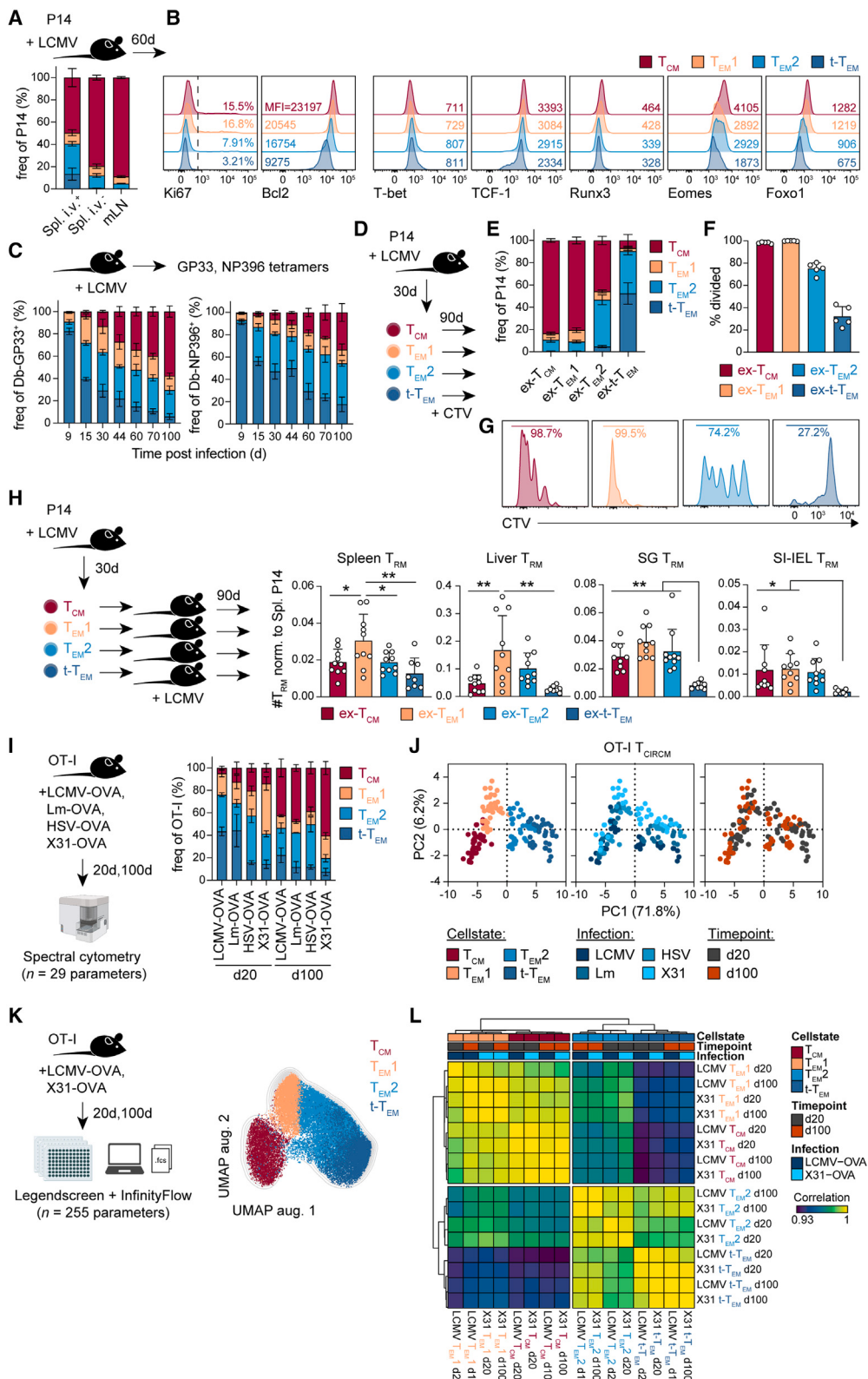
(E) Biplots of InfinityFlow predictions by early and late events based on pseudotime (top and bottom 20%). Markers expressed by early or late events highlighted in red and blue, respectively.

(F) One-SENSE dimensionality reduction of T_{CIRCM} cells using markers highlighted in (E).

(G) Conventional gating strategy of T_{CIRCM} populations. T_{CM} , T_{EM} , and t- T_{EM} cells overlaid on one-SENSE plot. T_{EM} cells were subdivided into two clusters based on one-SENSE representation.

(H) Heatmap representation of differentially expressed markers between T_{CIRCM} populations.

(I and J) (I) Manual gating strategy defining T_{CM} , T_{EM1} , T_{EM2} , and t- T_{EM} cells overlaid on (J) one-SENSE plot.



(legend on next page)

states (Figure 1G). In particular, cells comprising the T_{EM} cell subset could be broadly divided into at least two major subpopulations that appeared more memory-like (T_{EM1} cells; elevated expression of CD11c, CD55, CXCR3, HVEM, Ly108, and VISTA) or effector-like (T_{EM2} cells; elevated expression of CD18, CD54, CD94, CX3CR1, KLRG1, and NK1.1) (Figures 1G, 1H, and S1J). Hence, InfinityFlow uncovered extensive phenotypic heterogeneity and a nuanced continuum of differentiation states within the T_{CIRCM} cell pool.

T_{CIRCM} cells comprise discrete populations with graded differentiation potential, longevity, and tissue localization

To characterize the T_{CIRCM} cell pool beyond surface phenotype, we devised a gating strategy using four discriminating markers that recapitulated the definition of T_{CIRCM} populations via one-SENSE analysis. Specifically, this allowed us to distinguish CD62L⁻CXCR3⁺CD127⁺CX3CR1⁻ T_{EM1} cells from CD62L⁻CXCR3⁻CD127⁺CX3CR1⁺ T_{EM2} cells, in addition to CD62L⁺CXCR3⁺CD127⁺CX3CR1⁻ T_{CM} cells and CD62L⁻CXCR3⁻CD127⁻CX3CR1⁺ t-T_{EM} cells (Figures 1I and 1J). Using this identification strategy, we found that T_{CM} cells, and to a lesser extent T_{EM1} and T_{EM2} cells, could infiltrate lymphoid tissues, whereas t-T_{EM} cells were excluded from these niches (Figure 2A). Moreover, the reduced persistence of t-T_{EM} cells, as compared with T_{CM}, T_{EM1}, and T_{EM2} cells, was accompanied by progressively reduced levels of the proliferation marker Ki67; the anti-apoptotic factor Bcl2; and pro-memory transcription factors (TFs) TCF-1, Eomes, and Foxo1 (Figure 2B), suggesting a continuous survival advantage spanning from t-T_{EM} (most short-lived) to T_{CM} cells (most long-lived).

To understand the dynamics of these populations during memory T cell differentiation, we tracked GP33- and NP396-specific CD8⁺ T cells using tetramers following LCMV infection. As previously reported, t-T_{EM} cells rapidly contracted upon infection resolution.^{4,31} Comparatively, frequencies of T_{EM1} and T_{EM2} cells declined at a slower rate at the expense of T_{CM} cells that became the dominant population >100 dpi (Figure 2C), suggesting increased likelihood of T_{EM1} and T_{EM2} cells undergoing apoptosis or converting to the T_{CM} cell lineage over time.^{31,32,38} To determine stability and proliferative capacity, we sort-purified these populations 30 dpi. and labeled cells with CellTrace Violet (CTV) prior to transfer into

naive recipient mice (Figure 2D). Subsequently, 90 days later, we found that T_{CM} and t-T_{EM} cells exhibited the highest degree of stability in line with previous reports.^{4,31} While nearly all T_{EM1} cells converted into T_{CM} cells, T_{EM2} cells exhibited comparatively limited plasticity (Figure 2E). In addition, we found that while T_{CM} and T_{EM1} cells were highly proliferative, approximately 15% of T_{EM2} cells and 75% of t-T_{EM} cells remained undivided (Figures 2F and 2G). Finally, we investigated the capacity of T_{CIRCM} cells to form T_{RM} cells during secondary responses (Figure 2H). As anticipated, t-T_{EM} cells were largely defective in forming T_{RM} cells in all tested tissues, but interestingly, we found that T_{EM1} cells displayed enhanced differentiation into T_{RM} cells in the spleen and liver, compared with T_{CM} cells (Figure 2H). Overall, these analyses document the spectrum of differentiation states, tissue localization, and plasticity potential across the memory CD8⁺ T_{CIRCM} cell pool.

T_{CIRCM} cell states remain phenotypically stable across infection models and time

The kinetics of memory T cell differentiation can vary between epitope specificities and across different infection contexts for T cells sharing the same TCR.^{39,40} Having established that our T_{CIRCM} cell identification strategy could be employed to study longitudinal LCMV-specific GP33⁺ and NP396⁺ responses, we next examined if memory T cells differentiate through the same T_{CIRCM} cell states in response to diverse pathogens. To this end, we used ovalbumin (OVA₂₅₇₋₂₆₄)-specific OT-I T cells and recombinant pathogens expressing OVA (LCMV, *Listeria monocytogenes* [Lm], herpes simplex virus [HSV], and influenza virus [X31]) to enable the comparison of CD8⁺ T cell responses for a given antigen specificity. Analysis of OT-I T cells at early (20 days) or late (100 days) memory time points via high-dimensional spectral cytometry (Figure 2I; Table S3) revealed substantial differences in OT-I T cell phenotype at the population level over time, regardless of infection modality (Figures S2B and S2C).

However, upon deconvolution of the OT-I T_{CIRCM} population into T_{CM}, T_{EM1}, T_{EM2}, and t-T_{EM} cells, we observed that within a given state, the phenotype of memory T cells remained remarkably stable regardless of the pathogen or time point post infection (Figure 2J). To further validate this observation, we used the LEGENDScreen platform and InfinityFlow analysis

Figure 2. T_{CIRCM} cell states are phenotypically stable over time but differ in their plasticity and proliferation capacity

(A and B) Naive P14 CD45.1⁺ T cells were transferred into LCMV-infected recipients. Mice were administered with anti-CD8^β antibody i.v. to label vasculature-associated cells (i.v.⁺). (A) Frequency of T_{CIRCM} cells found in the spleen red pulp (i.v.⁺), white pulp (i.v.⁻), and mesenteric lymph nodes (mLNs) 60 dpi. (B) Expression of indicated molecules in P14 T_{CM}, T_{EM1}, T_{EM2}, and t-T_{EM} cells from the spleen 60 dpi. (C) Frequency of T_{CM}, T_{EM1}, T_{EM2}, and t-T_{EM} cells among splenic H-2D^b-GP33⁺ and H-2D^b-NP396⁺ cells, following LCMV infection at indicated time points. (D–G) Naive P14 CD45.1⁺ T cells were primed using LCMV. P14 T_{CM}, T_{EM1}, T_{EM2}, and t-T_{EM} cells were sort-purified 30 dpi, stained with CTV, transferred into naive recipients, and isolated from the spleen 90 days later. (E) Frequency of P14 T_{CIRCM} states originating from ex-T_{CM}, T_{EM1}, T_{EM2}, and t-T_{EM} cells. (F) Percentage of divided ex-T_{CM}, T_{EM1}, T_{EM2}, and t-T_{EM} cells assessed by CTV dilution and (G) representative flow cytometry plots. (H) Cells were sorted as in (D) and transferred into LCMV-infected recipients. T_{RM} cell numbers were quantified from indicated tissues 90 days later. (I–L) Naive OT-I CD45.1⁺ T cells were primed using LCMV-OVA, Lm-OVA, HSV-OVA, or X31-OVA and isolated from the spleen 20 or 100 dpi. (see Figures S2A–S2C and Table S3). (I) Frequency of T_{CM}, T_{EM1}, T_{EM2}, and t-T_{EM} cells for indicated infection models and time points. (J) PCA plots based on median expression profiles of OT-I T_{CIRCM} cell populations. (K and L) OT-I T cells were primed by LCMV-OVA or X31-OVA, isolated from the spleen 20 or 100 dpi and analyzed using LEGENDScreen and InfinityFlow (see Tables S2 and S4). Shown are (K) UMAP plot of T_{CIRCM} cell populations and (L) correlation matrix based on InfinityFlow-predicted median expression profiles for indicated populations, infection models, and time points. Data are representative of one out of two independent experiments in (A), (B), and (D)–(J) or pooled from two independent experiments in (C) and (H). In (A), (B), and (D)–(I) n = 3–5, and in (C), n = 3–7 per time point. Graphs show mean ± SD in (A), (E), (F), (H), and (I) or mean ± SEM in (C). In (H), *p < 0.05 and **p < 0.01, by one-way ANOVA.

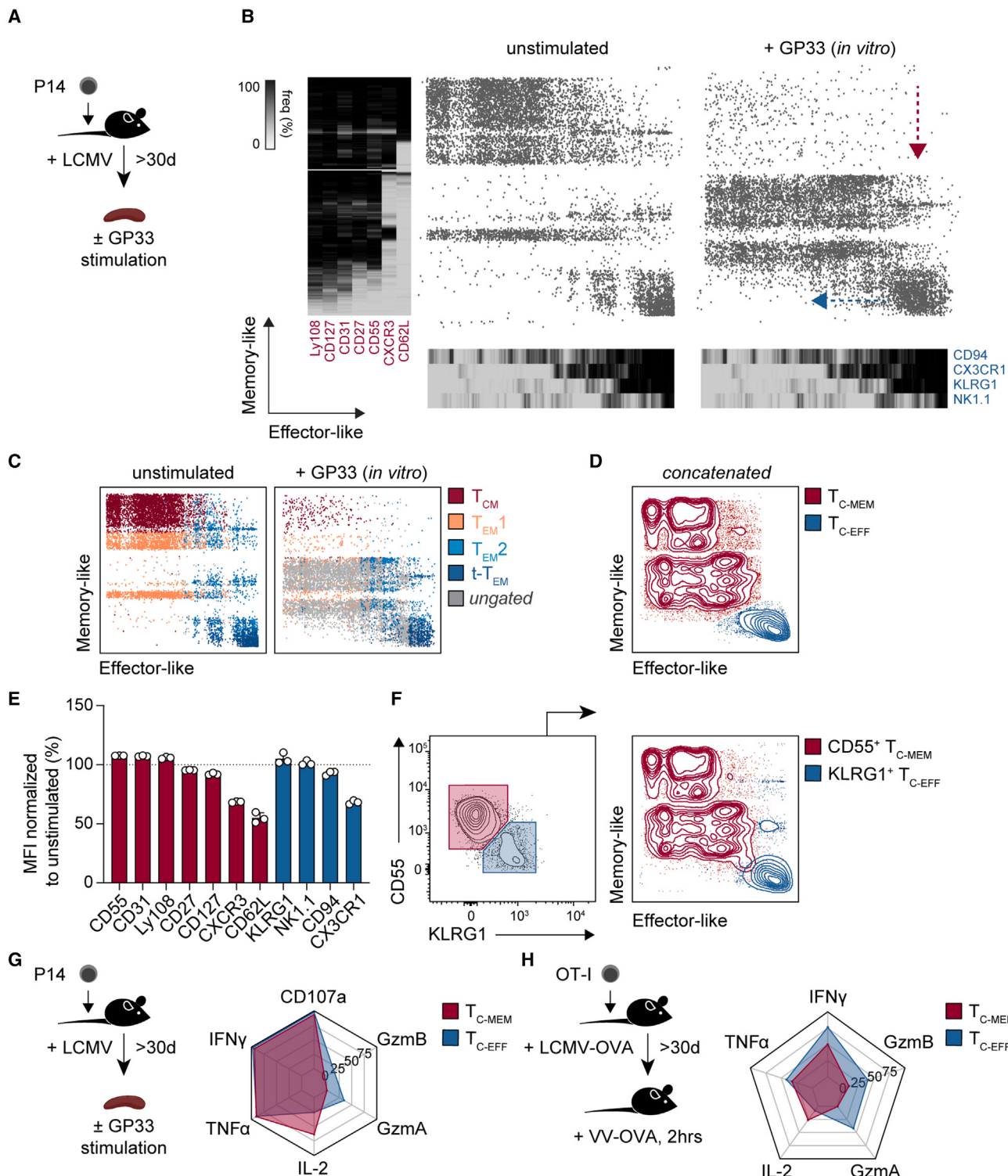


Figure 3. T_{CIRCM} cells can be subdivided into two main functional profiles

(A-D) Naive P14 CD45.1⁺ T cells were primed using LCMV, isolated from the spleen >30 days later, and stimulated *in vitro* with GP33 peptide. (B) One-SENSE dimensionality reduction. Memory-like or effector-like markers altered after stimulation are indicated with a red and a blue arrow, respectively. (C) T_{CIRCM} cell subsets were manually gated as in Figure 1I and were overlaid on one-SENSE plot. (D) Unstimulated and GP33-stimulated samples were concatenated and distinguished into memory-like T_{C-MEM} (red) or effector-like T_{C-EFF} (blue) clusters.

(E) Quantification of marker expression changes following GP33-stimulation in T_{C-MEM} or T_{C-EFF} clusters (see Figure S3B).

(F) Identification of T_{C-MEM} or T_{C-EFF} clusters using CD55 and KLRG1 (see Figure S3C).

(legend continued on next page)

to compare OT-I T_{CIRCM} cell differentiation following LCMV-OVA and X31-OVA infection (Figures 2K and S2E; Tables S2 and S4). While the composition of T_{CIRCM} populations was altered over time between infections (Figure 2I), surface proteomes remained similar within the same state across infection models and time (Figure 2L), such that LCMV-OVA-primed OT-I T_{CM} cells at 20 dpi more closely resembled X31-OVA-primed OT-I T_{CM} cells at 100 dpi, compared with other states.

One-SENSE analysis reveals the functional dichotomy of T_{CIRCM} cells

T cell functionality is often assessed via sort-purification of the subset of interest, followed by *in vitro* activation using various stimuli. However, such strategies are problematic given that markers used for subset identification, such as CD62L, fluctuate upon T cell reactivation.^{4,41} To address this issue, we employed one-SENSE analysis to evaluate the stability of T_{CIRCM} cell subset-defining markers, which as anticipated, revealed drastic shifts in marker expression upon *in vitro* peptide stimulation (Figures 3A and 3B). Such alterations of T_{CIRCM} cell-defining markers prevented identification of the T_{CIRCM} cell states defined above (Figures 1I and 3C). To circumvent this, we specified two broad T_{CIRCM} clusters as based on expression of memory or effector-like molecules (Figure 1F). We respectively termed these populations T_{C-MEM} cells (encompassing T_{CM} and T_{EM1} cells) and T_{C-EFF} cells (encompassing T_{EM2} and t-T_{EM} cells) (Figure 3D). This definition allowed us to quantify the relative abundance of surface markers within these two clusters following T cell reactivation. While the expression of CD62L, CXCR3, and CX3CR1 was diminished upon peptide stimulation, expression of other memory and effector-like surface markers remained stable (Figures 3E and S3A). Among these stable markers, CD55 and KLRG1 showed the highest staining index (Figure S3B), allowing for the identification of T_{C-MEM} and T_{C-EFF} populations within the T_{CIRCM} cell pool (Figures 3F and S3C).

This classification strategy allowed us to evaluate effector molecule production across T_{CIRCM} populations, whereby CD55⁺ T_{C-MEM} cells showed enhanced interleukin-2 (IL-2) production, and KLRG1⁺ T_{C-EFF} cells expressed elevated granzyme (Figure 3G). To determine if this functional stratification was conserved *in vivo*, we challenged LCMV-OVA immune mice containing OT-I T cells with OVA-expressing vaccinia virus (VV-OVA). Akin to *in vitro* stimulation, VV-OVA challenge led to decreased expression of CD62L, CXCR3, and CX3CR1 on OT-I cells, while CD55 and KLRG1 expression enabled T_{C-EFF} and T_{C-MEM} cell resolution (Figure 3H), with similar results observed after peptide, peptide-loaded dendritic cell (DC), or antigen-expressing recombinant adenovirus (rAAV) stimulation (Figures S3D–S3H). Additionally, OT-I T_{C-MEM} cells remained robust IL-2 producers, while T_{C-EFF} cells showed higher granzyme expression and IFN- γ and TNF- α production (Figure 3H). This contrasted with studies showing reduced effector cytokine production in sort-

purified terminally differentiated T_{CIRCM} cells following *in vitro* stimulation,^{4,42} thus highlighting potential sensitivity of discrete T_{CIRCM} populations downstream of cell-sorting procedures. Together, these results provide an systematic approach for the identification of stable markers enabling the functional assessment of T_{CIRCM} cell subsets.

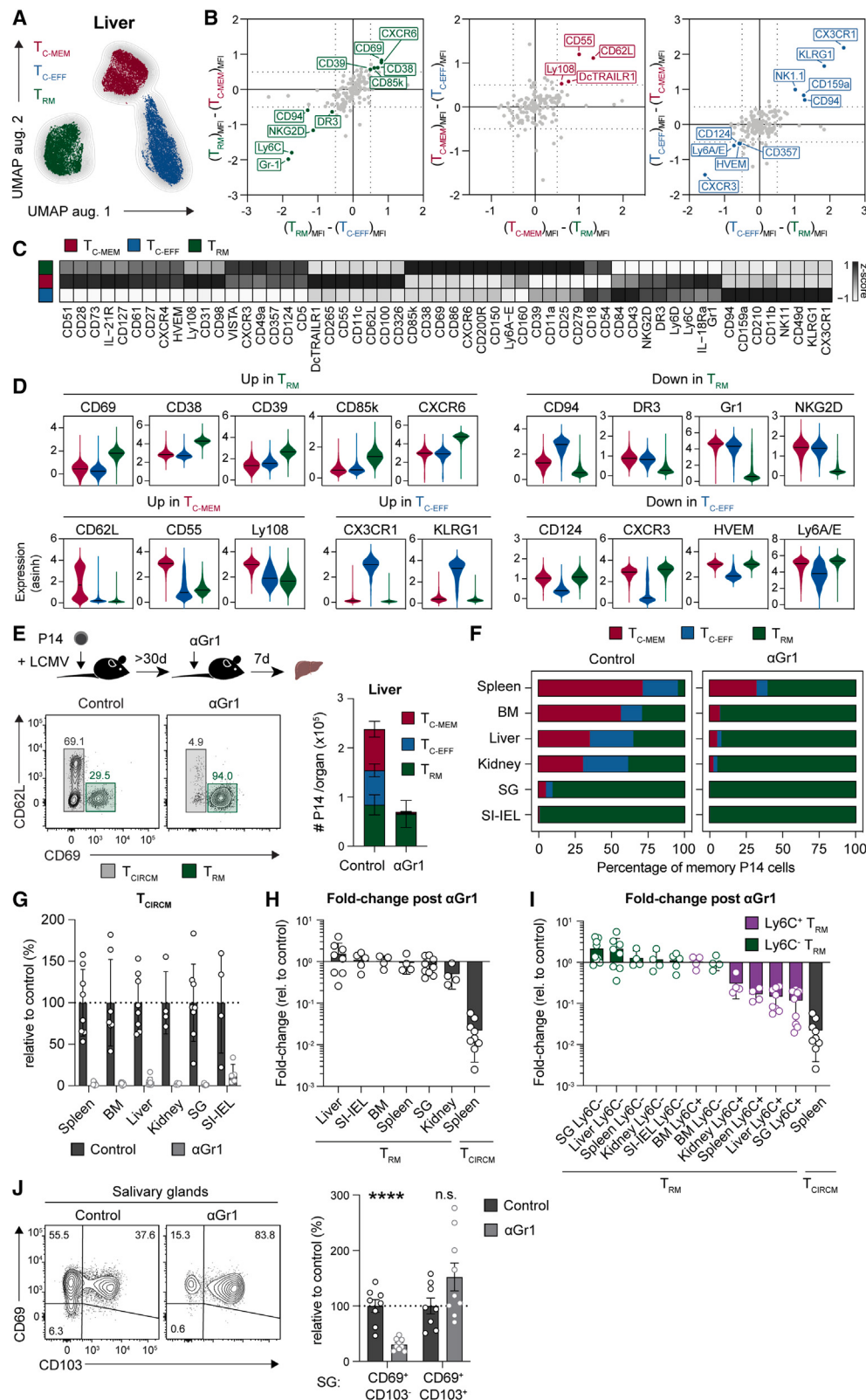
Surface proteome assessment allows segregation and targeted depletion of distinct CD8⁺ T cell states

The delineation of T_{CIRCM} and T_{RM} cells remains challenging, particularly in tissues where these subsets coexist. To identify additional markers enabling T_{CIRCM} and T_{RM} cell demarcation, we focused our analyses on the liver that contains various T cell states.^{11,43} UMAP analysis of liver memory CD8⁺ T cells, using InfinityFlow-generated predictions, revealed three major populations corresponding to T_{RM}, T_{C-MEM}, and T_{C-EFF} cells based on CD69, CD55, and KLRG1 expression, respectively (Figures 4A, S4A, and S4B). Analysis of differentially expressed markers revealed molecules induced or repressed in liver T_{RM}, T_{C-MEM}, and T_{C-EFF} populations (Figures 4B and 4C). Notably, liver T_{RM} cells expressed CD38, CD39, CD85k, and CXCR6 in addition to CD69, whereas CD94, DR3, Gr1, and NKG2D expression was unique to T_{C-MEM} and T_{C-EFF} cells (Figure 4D). Beyond the liver, this pattern of staining could also be recapitulated on T_{C-MEM} (CD55), T_{C-EFF} (CX3CR1, KLRG1), and T_{RM} (CD69, CD38, CD39, CXCR6) cells in the kidney (Figures S4B–S4E).

Depleting antibodies including anti-CD8 α or Thy1.1 have been employed to selectively eliminate T_{CIRCM} cells while preserving T_{RM} populations in the female reproductive tract (FRT), lung, and skin.^{18,44,45} However, these methods also deplete T_{RM} cells from highly vascularized tissues such as the liver.¹¹ Alternatively, anti-Gr1 or nicotinamide adenine dinucleotide (NAD⁺) treatment have been used to eliminate T_{CIRCM} or T_{RM} cells from the liver, respectively.^{43,46} Given the vast heterogeneity of T_{RM} cells across tissues, we postulated that the efficacy of these methods may differ between locations. For instance, T_{RM} cells in some organs express Gr1 (Figure S4G), while skin T_{RM} cells lack P2RX7, a receptor necessary for NAD⁺-induced cell death⁴⁶ (Figure S4H). Beyond the liver, we found that while anti-Gr1 treatment eliminated T_{CIRCM} cells in all organs examined, it also promoted the depletion of Ly6C⁺CD69⁺ T_{RM} cells, resulting in the partial removal of CD69⁺CD103[−] SG T_{RM} population (Figures 4E–4J). In contrast, NAD⁺-mediated T_{RM} cell depletion varied widely between sites, ranging from the eradication of SI-IEL T_{RM} cells, to skin T_{RM} cells being unaffected (Figures S4I–S4L). Collectively, these results illustrate the utility of these depletion regimes on T_{CIRCM} and T_{RM} cells across organs, highlighting that while these methods are well suited in the liver and SI-IEL, alternative strategies should be considered to eradicate skin T_{RM} cells.⁴⁷

(G) Mice were treated as in (A). Radar plot quantification of various effector molecules. CD107a, IFN- γ , TNF- α , and IL-2 were assessed after GP33-stimulation. GzmA and GzmB were quantified in unstimulated samples.

(H) Naive OT-I CD45.1⁺ T cells were primed using LCMV-OVA and challenged with VV-OVA >30 days later. Radar plot quantification of indicated effector molecules. Data are representative of one out of two independent experiments in (A)–(G) or one out of four independent experiments in (H), n = 3–4. Graphs show mean \pm SD.



(legend on next page)

CD103 expression status encapsulates phenotypic divergence of T_{RM} cells across tissues

While T_{RM} cells share a core transcriptional gene signature,^{29,48–50} external factors derived from the tissue microenvironment elicit organ-specific gene programs, allowing T cell adaptation to their tissue of residence.^{15,24,43,51} To explore organ-specific variations in T_{RM} cell phenotype, we performed UMAP analysis on the T_{RM} cluster using InfinityFlow-generated predictions (Figure 5A). Analysis of protein co-expression revealed that while T_{RM} cells from the spleen and liver appeared phenotypically similar, other populations such as those found in the SG and SI-IEL had more diverse expression profiles (Figures 5A and 5B). In particular, SI-IEL T_{RM} cells showed elevated expression of immunomodulatory receptors (CD160, CD223/LAG3) and lower expression of adhesion molecules (CD49a, CD49d, CD54), compared with T_{RM} cells found in other organs (Figures 5C and S5A). Interestingly, BM T_{RM} cells showed increased levels of markers typically found on endothelial (CD31, CD106) and myeloid cells (CD172a, F4/80, MHCII) (Figures 5C and S5A).

CD103 expression by T_{RM} cells is associated with epithelial localization, with CD103⁺ T_{RM} cells predominantly residing at these surfaces.^{15,18,52,53} Moreover, CD103 appears to denote T_{RM} populations with reduced functionality and participation in secondary immune responses.⁴³ To assess whether CD103 expression would partition the T_{RM} cell phenotypic heterogeneity observed above, we overlayed CD103 staining intensity on UMAP coordinates (Figures 5D and 5E). Segregating T_{RM} cells according to CD103 expression revealed phenotypic similarities between SG and SI-IEL CD103⁺ T_{RM} cells as compared with their CD103⁻ counterparts, which instead resembled T_{RM} cells found in other tissues (Figures 5F and 5G). Since CD103 is directly regulated by the cytokine TGF-β,^{48,54} we examined the extent to which TGF-β drives the heterogeneity between CD103⁺ and CD103⁻ T_{RM} cell subsets. Using OT-I T cells sufficient (WT) or deficient for TGF-βRII (*Tgfb2*^{-/-}), we found that TGF-βRII-deficient SG and SI-IEL T_{RM} cells bore phenotypic resemblance to WT cells from the BM, spleen, liver, and kidney (Figures S5B–S5D), highlighting TGF-β signaling as a major driver of T_{RM} cell phenotypic heterogeneity.

CXCR6 and CD38 enable T_{RM} cell characterization independently of CD69 expression

We next sought to investigate whether surface proteins identified by our dataset could demarcate T_{RM} from T_{CIRCM} cells across organs. To this end, we performed differential expression analysis

on InfinityFlow-generated predictions and identified markers that were highly expressed (including CXCR6, CD38, CD49a, CD85k, CD103, CD160) or repressed (including CD43_S11, CD55, CD122, DR3, Gr1, NKG2D) on T_{RM} cells compared with T_{CIRCM} cell subsets. While the presence of these markers on T_{RM} cells varied between tissues, the assignment of molecules to “circulation-associated” or “residency-associated” categories, revealed a clear demarcation between T_{CIRCM} and T_{RM} cells via one-SENSE analysis (Figures 6A and S6A). To validate the use of markers to distinguish T_{RM} cells, we utilized reporter mice expressing Hobit (*Hobit*^{Tom}), a TF specifically induced in murine T_{RM} cells.⁵⁰ Following LCMV infection (>30 dpi), the vast majority of Hobit-expressing LCMV-specific CD8⁺ T cells in the liver co-expressed CXCR6 and CD38 in addition to CD69, a pattern observed in other organs (Figure 6B). To further validate CXCR6 and CD38 as T_{RM} cell-defining markers, LCMV-immune mice (>30 dpi) were treated with anti-Gr1 to deplete T_{CIRCM} cells or NAD⁺ to induce T_{RM} cell death. Indeed, liver CXCR6⁺CD38⁺ cells were greatly enriched following T_{CIRCM} cell depletion via anti-Gr1, whereas these cells were lost after NAD⁺ administration (Figure S6B).

While CD69 is often used to identify T_{RM} cells under steady-state conditions, CD69 expression is highly dynamic and can be induced by a vast array of stimuli.^{15,16} For instance, CD69 induction by T_{CIRCM} cells can be detected following TCR stimulation or incubation with pro-inflammatory cytokines such as type I IFN or TNF-α (Figure S6C). A similar phenomenon was observed *in vivo* whereby OT-I T_{CIRCM} cells expressed CD69 in a dose-dependent manner upon exposure to VV-OVA. In contrast, CXCR6 and CD38 expression by T_{CIRCM} cells remained stable following VV-OVA challenge (Figure 6C).

We reasoned that CXCR6 and CD38 could be employed to demarcate T_{CIRCM} from T_{RM} cells independently of CD69 to better understand T_{RM} cell functional contributions during inflammatory stress. To this end, we challenged LCMV-OVA-immune mice (>30 dpi) with VV-OVA and assessed the production of effector molecules in liver OT-I T cells (Figure 6D). As expected, CD62L and CD69 expression was altered upon restimulation, with CD62L and CD69 being shed or induced, respectively (Figure 6D). In contrast, CXCR6 and CD38 expression remained similar following VV-OVA infection (Figures 6D and S6D) or after using other reactivation methods (Figures S6E and S6F), allowing for CD69-independent T_{RM} cell identification. Using this classification, CD69⁺ T cells showed increased cytokine production and decreased granzyme expression, whereas CD69⁺CXCR6⁺CD38⁺ liver T_{RM} cells showed enhanced production of IL-2 and granzyme B

Figure 4. Identification of discriminating markers between T_{CIRCM} and T_{RM} cells allows targeted depletion of discrete populations

(A–D) InfinityFlow analysis of liver memory T cells (see Figure 1). (A) UMAP analysis of liver P14 T cells using InfinityFlow-predictions (see Figure S4A). (B) Marker expression by liver T_{C-MEM}, T_{C-EFF}, and T_{RM} cell subsets. (C) Heatmap representation and (D) violin plots of differentially expressed markers in indicated populations.

(E–J) Mice received naive P14 CD45.1⁺ T cells, were infected with LCMV, and were treated with anti-Gr1 antibody >30 days later. P14 T cells were isolated from various organs 7 days later. (E) (Left) representative flow cytometry plots and (right) enumeration of liver T_{C-MEM}, T_{C-EFF}, and T_{RM} cells. (F) Frequency of memory P14 T cell subsets in control or anti-Gr1 antibody-treated mice across tissues. (G) T_{CIRCM} cell depletion efficacy after anti-Gr1 treatment relative to control mice in indicated tissues. (H and I) Numbers of (H) total P14 T_{RM} cells or (I) Ly6C⁺ or Ly6C⁻ CD69⁺ T_{RM} cells in indicated tissues or spleen T_{CIRCM} cells, following anti-Gr1 treatment normalized to controls. (J) Shown are (left) representative FACS plots and (right) quantification of SG T_{RM} cell subsets’ depletion after anti-Gr1 treatment relative to control mice. Data are representative of one out of two independent experiments in (E) and (F) or pooled from two independent experiments in (G)–(J). In (E) and (F), n = 4–5; in (G)–(J), n = 4–9. Graph shows mean ± SD. In (J), ***p < 0.0001, by unpaired t test.

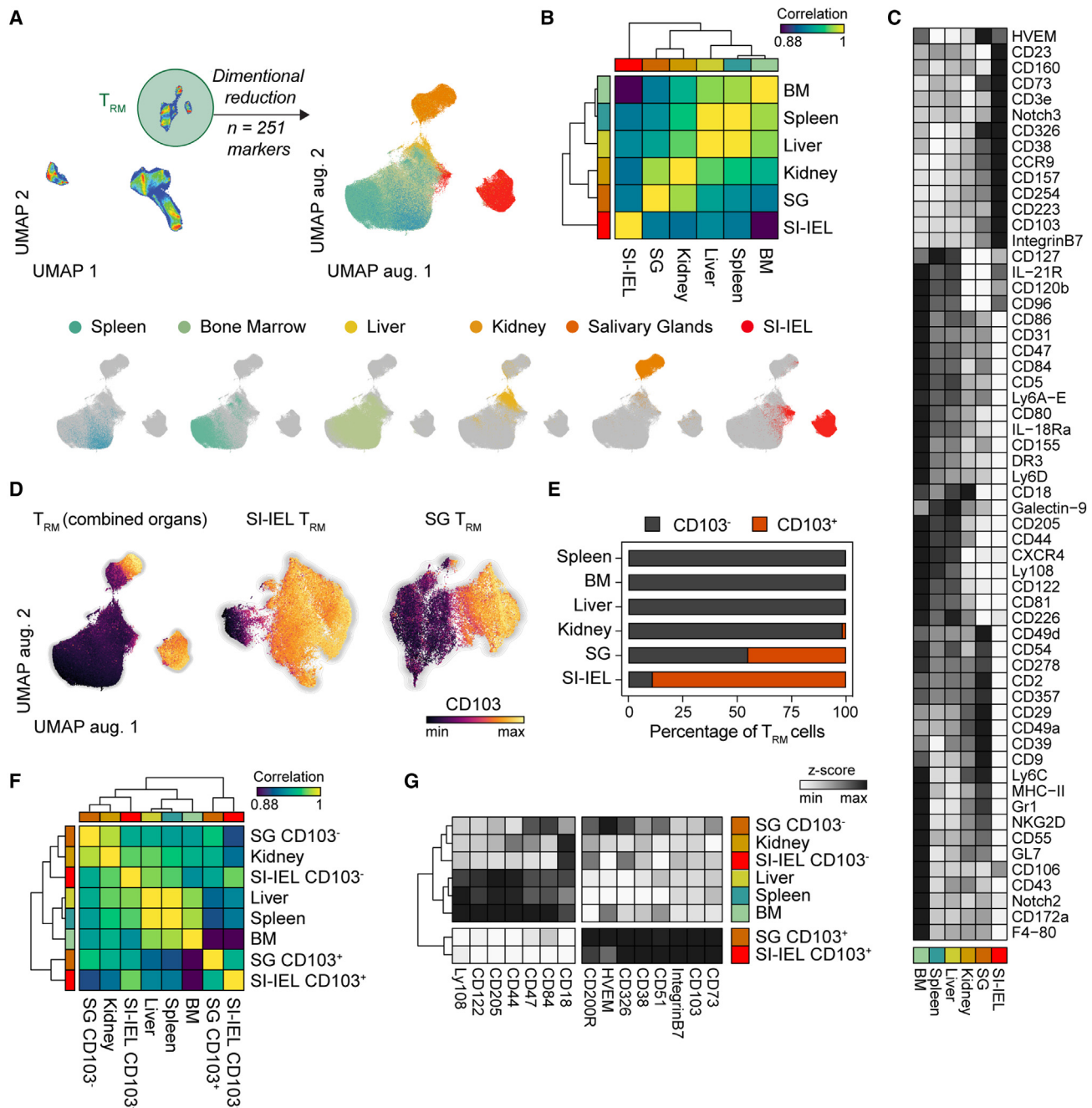


Figure 5. CD103 marks two tissue-resident phenotypic cell states across organs

(A) UMAP dimensionality reduction of T_{RM} cluster using InfinityFlow-predictions. Cells were colored by tissues (see Figure 1).

(B) Correlation matrix between T_{RM} cells from indicated tissues based on predicted median expression profiles.

(C) Heatmap representation of differentially expressed markers between T_{RM} cells from indicated tissues.

(D) UMAP plots generated using InfinityFlow predictions from combined T_{RM}, SI-IEL T_{RM}, or SG T_{RM} cells, colored with CD103 expression.

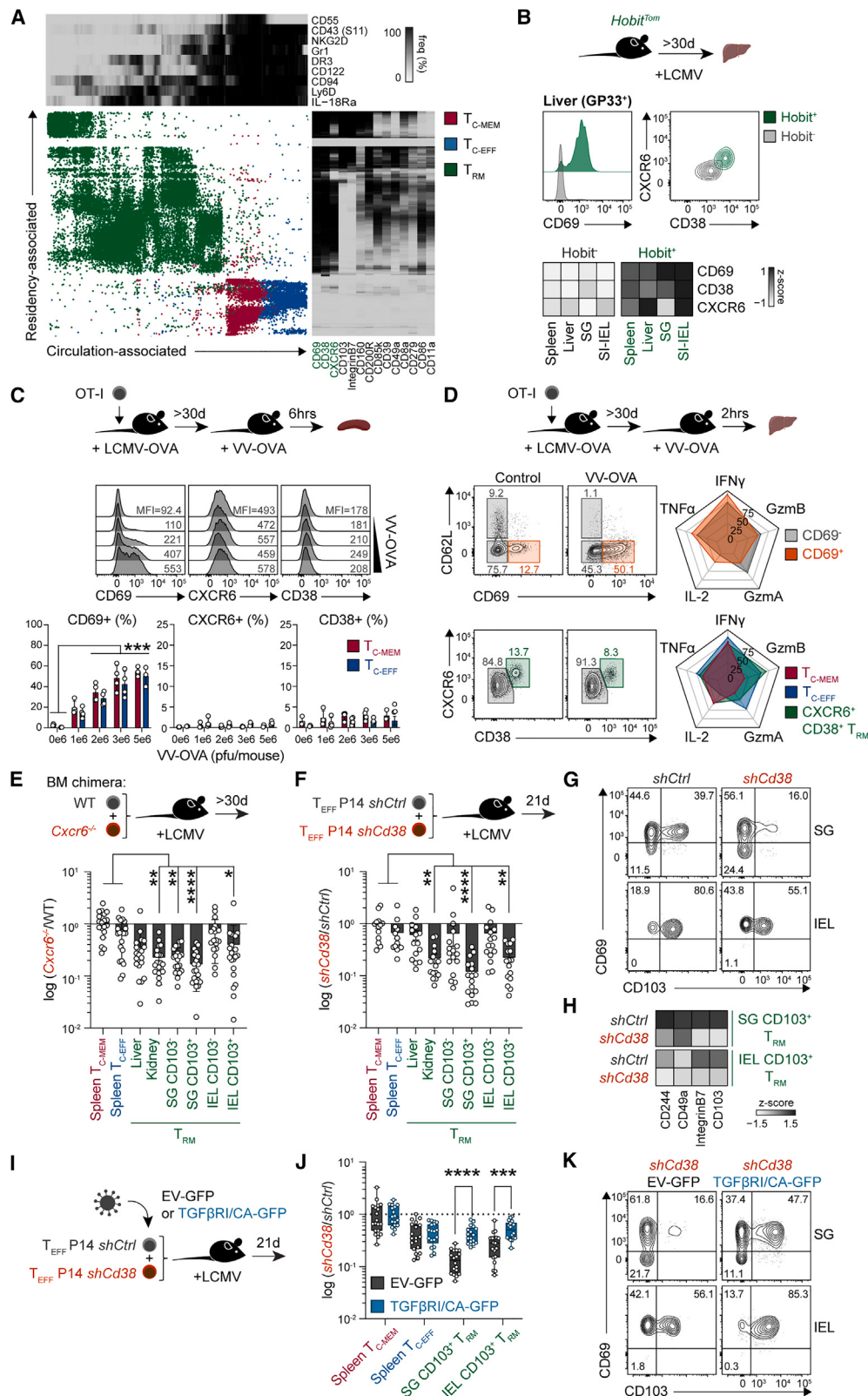
(E) Proportion of T_{RM} cells expressing CD103 in indicated tissues.

(F and G) SI-IEL and SG T_{RM} cells were subdivided according to CD103 expression. (F) Correlation matrix based on predicted median expression profiles of T_{RM} cells from various organs. (G) Heatmap representation of indicated markers in T_{RM} cells.

following VV-OVA infection (Figure 6D). Thus, employing CXCR6 and CD38 for T_{RM} cell identification enables the evaluation of their functionality during inflammation and antigen challenge, which cannot be achieved using CD69 expression alone.

CXCR6 and CD38 are required for T_{RM} cell development

Next, we investigated the functional relevance of CXCR6 and CD38 expression on T_{RM} cells. To address this, we generated mixed BM chimeric mice to delete Cxcr6 or used shRNA

**Figure 6.** T_{RM} cells can be identified by CXCR6 and CD38

(A and B) (A) One-SENSE analysis using residency- or circulation-associated markers, depicting T_{C-MEM} (red); T_{C-EFF} (blue); and T_{RM} cells pooled from spleen, BM, liver, kidney, SG, and SI-IEL (green) (see Figure S6A). (B) Hobit^{Tom} reporter mice were infected with LCMV; H-2D^b-GP33⁺ cells were isolated from indicated

(legend continued on next page)

retroviral vectors to knock down *Cd38*, before infecting recipient mice with LCMV (Figures 6E, 6F, and S6G). Loss of either one of these molecules resulted in decreased T_{RM} cell numbers in kidney, SG, and SI-IEL (Figures 6F and 6G). While CXCR6-deficiency has been associated with defective tissue T cell migration and retention in peripheral tissues,^{55,56} the functional relevance of CD38 in T_{RM} cell biology was unclear. Given that Sirt1 regulates CD4⁺ T cell differentiation in a manner downstream of CD38,⁵⁷ we reasoned that a similar mechanism may operate in T_{RM} cells. However, deletion of Sirt1 in CD38-ablated cells did not correct the T_{RM} cell differentiation defect found in the absence of CD38 (Figures S6H–S6J).

Since CD38 deletion specifically affected TGF-β-dependent CD103⁺ T_{RM} populations (Figure 6G), we postulated that CD38 may impact TGF-β responsiveness. Supporting this notion, CD38 expression appeared partially regulated by TGF-β (Figure S5D), while the loss of CD38 resulted in the reduced expression of TGF-β-associated molecules in CD103⁺ T_{RM} cells (Figure 6H). To demonstrate whether the CD38-mediated T_{RM} cell defect could be overcome by enhanced TGF-β signaling, we employed CD8⁺ T cells expressing a latent constitutively active form of TGF-β receptor (TGF-βRI/CA).⁵⁸ We found that TGF-βRI/CA expression was sufficient to restore CD103⁺ T_{RM} cell differentiation in CD38-ablated cells (Figures 6I–6K), suggesting that CD38 expression is required for TGF-β responsiveness, allowing CD103⁺ T_{RM} cell generation at epithelial sites. Collectively, our data indicate that CXCR6 and CD38 not only demarcate T_{RM} from T_{CIRCM} cells across organs, but also promote T_{RM} cell development.

A unified phenotypic signature identifies T_{RM} cells across tissues and infection models

While T_{RM} cells are shaped by tissue signals from the surrounding microenvironment,⁴³ T cell priming events can also impact T_{RM} cell differentiation.^{24,59,60} To assess the impact of different T cell activation contexts on T_{RM} cell phenotype, we comparatively assessed T_{RM} populations generated in response to distinct pathogens. To this end, we transferred naive OT-I T cells into mice infected with OVA-expressing pathogens (LCMV, Lm, HSV, or X31) and analyzed OT-I T cells across tissues via InfinityFlow (Figures 7A and S7A; Table S5). UMAP analysis of T_{RM} cells revealed two main populations segregated by CD103 expression, which was consistent

across infection models and antigen specificity (Figures 7B and 7C). We found that CD103⁺ T_{RM} cells in different tissues generated by either LCMV, Lm, HSV, or X31 infection were more similar to one another than their CD103⁻ counterparts found in the same tissue and generated by the same pathogen (Figure 7D). Moreover, the comparison of memory T cells primed by distinct pathogens within the same organ revealed that the surface proteome of T_{RM} populations was highly consistent across infection models (Figures 7E and S7C), suggesting that T_{RM} cell phenotype is predominantly driven by the tissue microenvironment.

Finally, one-SENSE analysis confirmed that circulation- and residency-associated phenotypic signatures derived from P14 T cells and LCMV-Armstrong infection could be extrapolated to other antigen (OVA) and pathogen contexts, thereby enabling the demarcation of T_{CIRCM} and T_{RM} cells in all tissues tested. In particular, a core set of surface molecules could be utilized to distinguish CD55⁺ T_{C-MEM} , KLRG1⁺ T_{C-EFF} , and T_{RM} cells (increased CD69, CXCR6, CD38, and CD85k and reduced CD55, CD43_S11, Gr1, and CD45RB, among others) across tissue sites and infection models (Figures 7F and S7D). Altogether, these results demonstrate the utility of our memory T cell surface protein atlas across various tissues and infection contexts, thereby enabling further exploration of memory T cell biology in health and disease.

DISCUSSION

Although the disparities between T_{CIRCM} and T_{RM} cells are increasingly appreciated,^{2,8,12} the disentanglement of these populations remains challenging. T_{RM} cells have been identified in virtually all tissue locations, including epithelial sites and solid organs such as the liver. At these locations, T_{RM} cells often lack CD103 expression and are commonly identified based on CD69 expression. Here, our InfinityFlow datasets uncovered two broad T_{RM} populations that could be distinguished based on TGF-β-driven CD103 expression, finding that CD103⁻ and TGF-βRII-deficient T_{RM} cells in epithelial locations phenotypically resembled those in non-epithelial sites. Notably, T_{RM} populations residing within the same tissue exhibit remarkable proteomic similarity regardless of the pathogen inducing T cell priming, suggesting that T_{RM} cell phenotypic adaptation is primarily governed by local niches. While further complexity

organs >30 days later and distinguished based on Hobit expression. (Top) Representative flow cytometry plots and (bottom) heatmaps of markers in indicated tissues.

(C) Naive OT-I CD45.1⁺ T cells were primed using LCMV-OVA, challenged with increasing titers of VV-OVA >30 dpi and isolated from the spleen. (Top) representative flow cytometry plots and (bottom) quantification of indicated markers.

(D) Mice were treated as in (C). (Left) representative flow cytometry plots and (right) quantification of effector molecules depicted as radar plots (see Figure S6D).

(E) WT and *Cxcr6*^{-/-} chimeric mice were infected with LCMV (see STAR Methods). Donor-derived (CD45.2⁺) H-2D^b-GP33⁺ cells were analyzed from indicated organs 30 dpi. Normalized ratios of *Cxcr6*^{-/-} and WT cells for indicated populations.

(F–H) Congenically distinct P14 T cells were transduced with control (*shCtrl*) or CD38 (*shCd38*) shRNA retroviruses and co-transferred in LCMV-infected recipients (see Figure S6H). Transduced cells were isolated from various tissues 21 days post-transfer. (F) Normalized ratios of *shCd38* and *shCtrl* cells for indicated populations, (G) representative flow cytometry plots, and (H) heatmap representation of markers.

(I–K) Congenically distinct P14 T cells were co-transduced with *shCtrl* or *shCd38* shRNA retroviruses and an empty (EV-GFP) or TGF-βRI/CA (TGF-βRI/CA-GFP) expression vector. Transduced P14 T cells were transferred in LCMV-infected recipients and isolated from indicated tissues 21 days post-transfer. (J) Normalized ratios of *shCd38* and *shCtrl* cells for indicated populations and (K) representative flow cytometry plots. Data are representative of one out of two independent experiments in (B), one out of three independent experiments in (C) and (D), or pooled from two independent experiments in (E)–(K). In (B), n = 5 per group; in (C) and (D), n = 3–4 per group; in (E), n = 9 per group; and in (E)–(K), n = 15–20 per group. Graphs show mean ± SD in (C) or mean ± SEM in (E), (F), and (J). *p < 0.05, **p < 0.01, ***p < 0.001, and ****p < 0.0001 in (C) and (I) by two-way ANOVA or in (E) and (F) by one-way ANOVA.

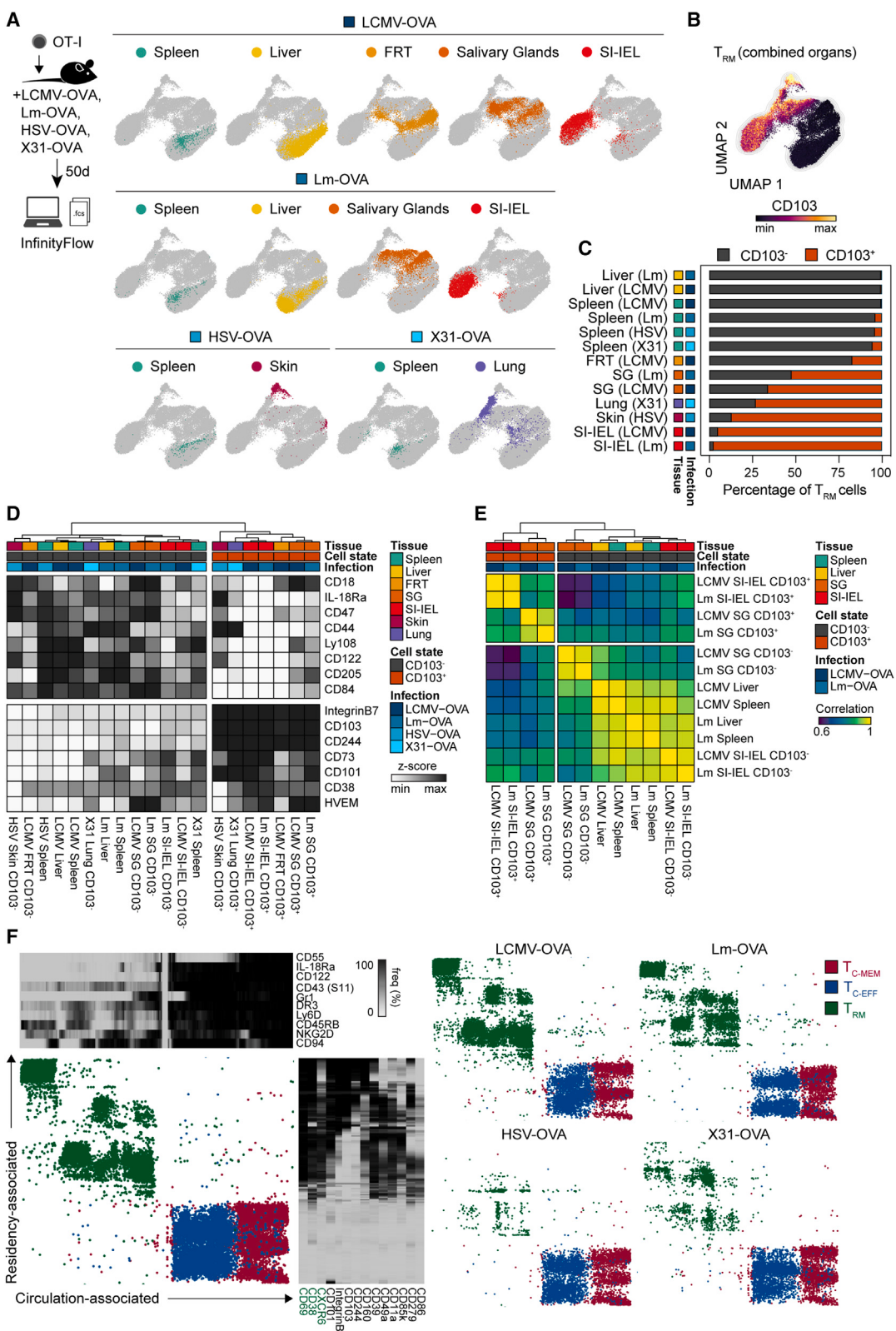


Figure 7. Phenotypic demarcation of T_{CIRCM} and T_{RM} cell states across tissues and infection models

(A–F) Naive OT-I CD45.1⁺ T cells were primed using LCMV-OVA, Lm-OVA, HSV-OVA, or X31-OVA, isolated from indicated organs 50 dpi and analyzed using InfinityFlow. (A and B) UMAP dimensionality reduction of T_{RM} cluster (see Figures S7A and S7B and Table S5), (A) colored according to the tissue of origin or

(legend continued on next page)

likely exists within CD103⁻ and CD103⁺ populations, as evidenced by studies identifying a subdivision of SI-IEL T_{RM} cells to include Id3⁺ memory-like and Blimp1⁺ effector-like subsets.^{20,61} These populations could not be discerned in our dataset, possibly due to the decline of Blimp1-expressing cells during the memory contraction phase.⁶¹

While CD69 expression on T_{RM} cells is stable under homeostatic conditions, expression of this molecule is dynamically regulated on T_{CIRCM} cells upon reactivation. Additionally, CD69⁻ cells have been identified as resident based on their migratory behavior, using parabiosis surgery,⁶² which suggests that T_{RM} cell identification requires additional markers. Here, we revealed a suite of markers that allows for demarcation of T_{RM} cells across tissues and infection models, including CXCR6 and CD38. Unlike CD69, both CD38 and CXCR6 were stably expressed under inflammatory conditions, allowing for the faithful delineation of T_{RM} cell effector capabilities. Moreover, CXCR6 and CD38 were required for efficient T_{RM} cell generation, especially among TGF- β -dependent CD103⁺ T_{RM} cells. Functionally, CD38 controls NAD⁺ local concentration by metabolizing it into ADPR. Since CD38 shields invariant NKT cells from NAD⁺-induced cell death via the ART2.2/P2RX7 pathway,⁶³ we hypothesized that a similar mechanism occurred in T_{RM} cells, although we did not find evidence that CD38 deletion induced T_{RM} cell apoptosis via this pathway (data not shown). Instead, we found that constitutive TGF- β signaling partially restores CD103⁺ T_{RM} cell differentiation in CD38-ablated cells, suggesting that CD38 potentiates TGF- β sensitivity.

While the complexity and heterogeneity of T_{CIRCM} cells is widely recognized,^{3,4,31} our study sheds light on the more nuanced continuum within this population. Although long-lived T_{CM} cells and t-T_{EM} cells comprise the most divergent populations within the T_{CIRCM} cell pool,^{3,4,31} we observed a spectrum of intermediate states that we categorized into T_{EM1} and T_{EM2} cells, which more closely resembled T_{CM} or t-T_{EM} cells, respectively, as based on their surface proteome. However, in comparison with t-T_{EM} cells, both T_{EM1} and T_{EM2} cell populations appeared to constitute *bona fide* memory T cells with regard to anatomical location, expression of pro-memory TFs, survival characteristics, and their capacity to generate T_{RM} cells during secondary responses. Additionally, while we identified T_{CIRCM} plasticity ranging from minimal t-T_{EM}-to-T_{CM} cell conversion to near complete of T_{EM1}-to-T_{CM} cell transdifferentiation, we found that T_{CIRCM} cells within each state retained a consistent phenotype across infection models and time.

In summary, here we created a comprehensive map of memory CD8⁺ T cell phenotype across murine tissues and infection models, with a view that this resource may facilitate future studies of T cell characterization and function. InfinityFlow is compatible with fluorescent reporters and TF staining,²⁷ allowing for flexible and deeper assessment of cell types of interest.^{28,64} While our study was designed to dissect CD8⁺ T cell phenotypic diversity, we envision that this workflow could be applied to a multitude of immune populations and

disease contexts in humans and mice for improved cell identification and the development of future diagnostics.

Limitations of the study

The InfinityFlow methodology requires the design of a comprehensive backbone antibody panel allowing the identification of relevant cell lineages to generate accurate predictions. While we have used extensive backbone panels containing common memory T cell classification markers, we cannot exclude further phenotypic diversity within these populations. Also, in this study we primarily employed TCR transgenic T cells for CD8⁺ T cell characterization, which do not fully recapitulate the breadth of CD8⁺ T cell responses toward a given pathogen. As such, T cells with differing TCR affinities or non-canonical CD8⁺ T cell lineages, such as Qa-1- or H2-M3-restricted populations present within endogenous T cells, were not characterized. Lastly, while we found that CD38 was necessary for CD103⁺ T_{RM} cell differentiation by potentiating TGF- β sensitivity, the absence of CD38 could not be fully rescued by constitutive TGF- β signaling, suggesting this molecule likely engages additional mechanisms to regulate T_{RM} cell formation.

STAR★METHODS

Detailed methods are provided in the online version of this paper and include the following:

- KEY RESOURCES TABLE
- RESOURCE AVAILABILITY
 - Lead contact
 - Materials availability
 - Data and code availability
- EXPERIMENTAL MODEL AND SUBJECT DETAILS
 - Mice
- METHOD DETAILS
 - T cell transfer
 - Infections
 - *In vivo* treatments
 - Mouse tissue processing
 - Flow cytometry
 - LEGENDScreen and InfinityFlow analysis
 - Dimensionality reduction, correlation and trajectory inference
 - Generation of murine BM-derived DCs
 - T cells stimulations and cytokine staining
 - CRISPR/Cas9 gene editing of CD8⁺ T cells
 - qPCR
 - Retroviral transduction of CD8⁺ T cells
- QUANTIFICATION AND STATISTICAL ANALYSIS

SUPPLEMENTAL INFORMATION

Supplemental information can be found online at <https://doi.org/10.1016/j.imuni.2023.06.005>.

(B) with CD103 expression. (C) Proportion of T_{RM} cells expressing CD103 in indicated tissues and infections. (D) Heatmap representation of indicated markers in T_{RM} cells. (E) Correlation matrix based on backbone and InfinityFlow-predicted median expression profiles of T_{RM} cell populations for indicated infections and organs. (F) One-SENSE analysis using residency- or circulation-associated markers depicting T_{C-MEM} (red); T_{C-EFF} (blue); and T_{RM} cells pooled from spleen, liver, FRT, SG, SI-IEL, lung, and skin (green) for indicated infection models (see Figure S7D).

ACKNOWLEDGMENTS

We thank Brooke Davies, Keely McDonald, and Natasha Zamudio for expert technical assistance. We thank the Melbourne Cytometry Platform from the Peter Doherty Institute for assistance with cell sorting. This work was supported by a Howard Hughes Medical Institute and Bill and Melinda Gates Foundation International Research Scholarship OPP1175796 to L.K.M. and an Australian Research Council grant DP200102753 to L.K.M. and M.E. L.K.M. is a senior medical research fellow supported by the Sylvia and Charles Viertel Charitable Foundation and an NHMRC Leadership Investigator Grant.

AUTHOR CONTRIBUTIONS

Conceptualization, M.E. and L.K.M.; investigation, M.E., R.F., A.O., S.L.P., N.G.-Z., S.N.C., J.L., T.N.B., A.C., and I.G.H.; formal analysis, M.E. and E.B.; software, M.E., E.B., J.S., and D.S.; writing – original draft, M.E. and L.K.M.; writing – review & editing, M.E., A.O., S.L.P., R.F., S.N.C., A.K., S.N.M., and L.K.M.; visualization, M.E., E.B., and L.K.M.; resources, P.B., A.K., F.G., R.G., and E.W.N.; funding acquisition, L.K.M.; supervision, L.K.M.

DECLARATION OF INTERESTS

The authors declare no competing interests.

INCLUSION AND DIVERSITY

We support inclusive, diverse, and equitable conduct of research.

Received: March 2, 2022

Revised: March 8, 2023

Accepted: June 7, 2023

Published: June 30, 2023

REFERENCES

1. Masopust, D., and Soerens, A.G. (2019). Tissue-resident T cells and other resident leukocytes. *Annu. Rev. Immunol.* 37, 521–546. <https://doi.org/10.1146/annurev-immunol-042617-053214>.
2. Mueller, S.N., and Mackay, L.K. (2016). Tissue-resident memory T cells: local specialists in immune defence. *Nat. Rev. Immunol.* 16, 79–89. <https://doi.org/10.1038/nri.2015.3>.
3. Renkema, K.R., Huggins, M.A., Borges da Silva, H., Knutson, T.P., Henzler, C.M., and Hamilton, S.E. (2020). KLRG1(+) memory CD8 T cells combine properties of short-lived effectors and long-lived memory. *J. Immunol.* 205, 1059–1069. <https://doi.org/10.4049/jimmunol.1901512>.
4. Milner, J.J., Nguyen, H., Omilusik, K., Reina-Campos, M., Tsai, M., Toma, C., Delpoux, A., Boland, B.S., Hedrick, S.M., Chang, J.T., et al. (2020). Delineation of a molecularly distinct terminally differentiated memory CD8 T cell population. *Proc. Natl. Acad. Sci. USA* 117, 25667–25678. <https://doi.org/10.1073/pnas.2008571117>.
5. Olson, J.A., McDonald-Hyman, C., Jameson, S.C., and Hamilton, S.E. (2013). Effector-like CD8(+) T cells in the memory population mediate potent protective immunity. *Immunity* 38, 1250–1260. <https://doi.org/10.1016/j.jimmuni.2013.05.009>.
6. Chang, J.T., Wherry, E.J., and Goldrath, A.W. (2014). Molecular regulation of effector and memory T cell differentiation. *Nat. Immunol.* 15, 1104–1115. <https://doi.org/10.1038/ni.3031>.
7. Jameson, S.C., and Masopust, D. (2018). Understanding subset diversity in T cell memory. *Immunity* 48, 214–226. <https://doi.org/10.1016/j.jimmuni.2018.02.010>.
8. Chung, H.K., McDonald, B., and Kaech, S.M. (2021). The architectural design of CD8+ T cell responses in acute and chronic infection: parallel structures with divergent fates. *J. Exp. Med.* 218. <https://doi.org/10.1084/jem.20201730>.
9. Shin, H., and Iwasaki, A. (2012). A vaccine strategy that protects against genital herpes by establishing local memory T cells. *Nature* 491, 463–467. <https://doi.org/10.1038/nature11522>.
10. Sheridan, B.S., Pham, Q.M., Lee, Y.T., Cauley, L.S., Puddington, L., and Lefrançois, L. (2014). Oral infection drives a distinct population of intestinal resident memory CD8(+) T cells with enhanced protective function. *Immunity* 40, 747–757. <https://doi.org/10.1016/j.jimmuni.2014.03.007>.
11. Fernandez-Ruiz, D., Ng, W.Y., Holz, L.E., Ma, J.Z., Zaid, A., Wong, Y.C., Lau, L.S., Mollard, V., Cozijnsen, A., Collins, N., et al. (2016). Liver-resident memory CD8(+) T cells form a front-line defense against malaria liver-stage infection. *Immunity* 45, 889–902. <https://doi.org/10.1016/j.jimmuni.2016.08.011>.
12. Milner, J.J., and Goldrath, A.W. (2018). Transcriptional programming of tissue-resident memory CD8(+) T cells. *Curr. Opin. Immunol.* 51, 162–169. <https://doi.org/10.1016/j.co.2018.03.017>.
13. Rissiek, B., Haag, F., Boyer, O., Koch-Nolte, F., and Adriouch, S. (2015). P2X7 on mouse T cells: one channel, many functions. *Front. Immunol.* 6, 204. <https://doi.org/10.3389/fimmu.2015.00204>.
14. Borges da Silva, H., Wang, H., Qian, L.J., Hogquist, K.A., and Jameson, S.C. (2019). ARTC2.2/P2RX7 signaling during cell isolation distorts function and quantification of tissue-resident CD8(+) T cell and invariant NKT subsets. *J. Immunol.* 202, 2153–2163. <https://doi.org/10.4049/jimmunol.1801613>.
15. Casey, K.A., Fraser, K.A., Schenkel, J.M., Moran, A., Abt, M.C., Beura, L.K., Lucas, P.J., Artis, D., Wherry, E.J., Hogquist, K., et al. (2012). Antigen-independent differentiation and maintenance of effector-like resident memory T cells in tissues. *J. Immunol.* 188, 4866–4875. <https://doi.org/10.4049/jimmunol.1200402>.
16. Skon, C.N., Lee, J.Y., Anderson, K.G., Masopust, D., Hogquist, K.A., and Jameson, S.C. (2013). Transcriptional downregulation of S1pr1 is required for the establishment of resident memory CD8+ T cells. *Nat. Immunol.* 14, 1285–1293. <https://doi.org/10.1038/ni.2745>.
17. Schenkel, J.M., Fraser, K.A., Casey, K.A., Beura, L.K., Pauken, K.E., Vezys, V., and Masopust, D. (2016). IL-15-independent maintenance of tissue-resident and boosted effector memory CD8 T cells. *J. Immunol.* 196, 3920–3926. <https://doi.org/10.4049/jimmunol.1502337>.
18. Mackay, L.K., Wynne-Jones, E., Freestone, D., Pellicci, D.G., Mielke, L.A., Newman, D.M., Braun, A., Masson, F., Kallies, A., Belz, G.T., et al. (2015). T-box transcription factors combine with the cytokines TGF-beta and IL-15 to control tissue-resident memory T cell fate. *Immunity* 43, 1101–1111. <https://doi.org/10.1016/j.jimmuni.2015.11.008>.
19. Watanabe, R., Gehad, A., Yang, C., Scott, L.L., Teague, J.E., Schlapbach, C., Elco, C.P., Huang, V., Matos, T.R., Kupper, T.S., et al. (2015). Human skin is protected by four functionally and phenotypically discrete populations of resident and recirculating memory T cells. *Sci. Transl. Med.* 7, 279ra39. <https://doi.org/10.1126/scitranslmed.3010302>.
20. Kurd, N.S., He, Z., Louis, T.L., Milner, J.J., Omilusik, K.D., Jin, W., Tsai, M.S., Widjaja, C.E., Kanbar, J.N., Olvera, J.G., et al. (2020). Early precursors and molecular determinants of tissue-resident memory CD8(+) T lymphocytes revealed by single-cell RNA sequencing. *Sci. Immunol.* 5. <https://doi.org/10.1126/scimmunol.aaz6894>.
21. Snyder, M.E., Finlayson, M.O., Connors, T.J., Dogra, P., Senda, T., Bush, E., Carpenter, D., Marboe, C., Benvenuto, L., Shah, L., et al. (2019). Generation and persistence of human tissue-resident memory T cells in lung transplantation. *Sci. Immunol.* 4. <https://doi.org/10.1126/scimmunol.aa5581>.
22. Savas, P., Virassamy, B., Ye, C., Salim, A., Mintoff, C.P., Caramia, F., Salgado, R., Byrne, D.J., Teo, Z.L., Dushyanthen, S., et al. (2018). Single-cell profiling of breast cancer T cells reveals a tissue-resident memory subset associated with improved prognosis. *Nat. Med.* 24, 986–993. <https://doi.org/10.1038/s41591-018-0078-7>.
23. Chen, Y., Shen, J., Kasmani, M.Y., Topchyan, P., and Cui, W. (2021). Single-cell transcriptomics reveals core regulatory programs that determine the heterogeneity of circulating and tissue-resident memory CD8(+) T cells. *Cells* 10. <https://doi.org/10.3390/cells10082143>.
24. Kok, L., Dijkgraaf, F.E., Urbanus, J., Bresser, K., Vredevoogd, D.W., Cardoso, R.F., Perié, L., Beltman, J.B., and Schumacher, T.N. (2020). A committed tissue-resident memory T cell precursor within the circulating

- CD8+ effector T cell pool. *J. Exp. Med.* 217. <https://doi.org/10.1084/jem.20191711>.
25. Mair, F., Erickson, J.R., Voillet, V., Simoni, Y., Bi, T., Tyznik, A.J., Martin, J., Gottardo, R., Newell, E.W., and Prlic, M. (2020). A targeted multi-omic analysis approach measures protein expression and low-abundance transcripts on the single-cell level. *Cell Rep.* 31, 107499. <https://doi.org/10.1016/j.celrep.2020.03.063>.
26. Schwanhäusser, B., Busse, D., Li, N., Dittmar, G., Schuchhardt, J., Wolf, J., Chen, W., and Selbach, M. (2011). Global quantification of mammalian gene expression control. *Nature* 473, 337–342. <https://doi.org/10.1038/nature10098>.
27. Becht, E., Tolstrup, D., Dutertre, C.A., Morawski, P.A., Campbell, D.J., Ginhoux, F., Newell, E.W., Gottardo, R., and Headley, M.B. (2021). High-throughput single-cell quantification of hundreds of proteins using conventional flow cytometry and machine learning. *Sci. Adv.* 7, eabg0505. <https://doi.org/10.1126/sciadv.abg0505>.
28. Dutertre, C.A., Becht, E., Irac, S.E., Khalilnezhad, A., Narang, V., Khalilnezhad, S., Ng, P.Y., van den Hoogen, L.L., Leong, J.Y., Lee, B., et al. (2019). Single-cell analysis of human mononuclear phagocytes reveals subset-defining markers and identifies circulating inflammatory dendritic cells. *Immunity* 51, 573–589.e8. <https://doi.org/10.1016/j.jimmuni.2019.08.008>.
29. Milner, J.J., Toma, C., Yu, B., Zhang, K., Omilusik, K., Phan, A.T., Wang, D., Getzler, A.J., Nguyen, T., Crotty, S., et al. (2017). Runx3 programs CD8(+) T cell residency in non-lymphoid tissues and tumours. *Nature* 552, 253–257. <https://doi.org/10.1038/nature24993>.
30. Becht, E., McInnes, L., Healy, J., Dutertre, C.A., Kwok, I.W.H., Ng, L.G., Ginhoux, F., and Newell, E.W. (2018). Dimensionality reduction for visualizing single-cell data using UMAP. *Nat. Biotechnol.* <https://doi.org/10.1038/nbt.4314>.
31. Gerlach, C., Moseman, E.A., Loughhead, S.M., Alvarez, D., Zwijnenburg, A.J., Waanders, L., Garg, R., de la Torre, J.C., and von Andrian, U.H. (2016). The chemokine receptor CX3CR1 defines three antigen-experienced CD8 T cell subsets with distinct roles in immune surveillance and homeostasis. *Immunity* 45, 1270–1284. <https://doi.org/10.1016/j.jimmuni.2016.10.018>.
32. Herndler-Brandstetter, D., Ishigame, H., Shinnakasu, R., Plajer, V., Stecher, C., Zhao, J., Lietzenmayer, M., Kroehling, L., Takumi, A., Kometani, K., et al. (2018). KLRLG1(+) effector CD8(+) T cells lose KLRLG1, differentiate into all memory T cell lineages, and convey enhanced protective immunity. *Immunity* 48, 716–729.e8. <https://doi.org/10.1016/j.jimmuni.2018.03.015>.
33. Bendall, S.C., Davis, K.L., Amir el, A.D., Tadmor, M.D., Simonds, E.F., Chen, T.J., Shenfeld, D.K., Nolan, G.P., and Pe'er, D. (2014). Single-cell trajectory detection uncovers progression and regulatory coordination in human B cell development. *Cell* 157, 714–725. <https://doi.org/10.1016/j.cell.2014.04.005>.
34. Cheng, Y., Wong, M.T., van der Maaten, L., and Newell, E.W. (2016). Categorical analysis of human T cell heterogeneity with one-dimensional soli-expression by nonlinear stochastic embedding. *J. Immunol.* 196, 924–932. <https://doi.org/10.4049/jimmunol.1501928>.
35. Friebel, E., Kapolou, K., Unger, S., Núñez, N.G., Utz, S., Rushing, E.J., Regli, L., Weller, M., Greter, M., Tugues, S., et al. (2020). Single-cell mapping of human brain cancer reveals tumor-specific instruction of tissue-invading leukocytes. *Cell* 181, 1626–1642.e20. <https://doi.org/10.1016/j.cell.2020.04.055>.
36. Bachmann, M.F., Wolint, P., Schwarz, K., Jäger, P., and Oxenius, A. (2005). Functional properties and lineage relationship of CD8+ T cell subsets identified by expression of IL-7 receptor alpha and CD62L. *J. Immunol.* 175, 4686–4696. <https://doi.org/10.4049/jimmunol.175.7.4686>.
37. Huster, K.M., Busch, V., Schiemann, M., Linkemann, K., Kerksiek, K.M., Wagner, H., and Busch, D.H. (2004). Selective expression of IL-7 receptor on memory T cells identifies early CD40L-dependent generation of distinct CD8+ memory T cell subsets. *Proc. Natl. Acad. Sci. USA* 101, 5610–5615. <https://doi.org/10.1073/pnas.0308054101>.
38. Youngblood, B., Hale, J.S., Kissick, H.T., Ahn, E., Xu, X., Wieland, A., Araki, K., West, E.E., Ghoneim, H.E., Fan, Y., et al. (2017). Effector CD8 T cells dedifferentiate into long-lived memory cells. *Nature* 552, 404–409. <https://doi.org/10.1038/nature25144>.
39. Sarkar, S., Teichgräber, V., Kalia, V., Polley, A., Masopust, D., Harrington, L.E., Ahmed, R., and Wherry, E.J. (2007). Strength of stimulus and clonal competition impact the rate of memory CD8 T cell differentiation. *J. Immunol.* 179, 6704–6714. <https://doi.org/10.4049/jimmunol.179.10.6704>.
40. Mueller, S.N., Langley, W.A., Li, G., García-Sastre, A., Webby, R.J., and Ahmed, R. (2010). Qualitatively different memory CD8+ T cells are generated after lymphocytic choriomeningitis virus and influenza virus infections. *J. Immunol.* 185, 2182–2190. <https://doi.org/10.4049/jimmunol.1001142>.
41. Huster, K.M., Koffler, M., Stemberger, C., Schiemann, M., Wagner, H., and Busch, D.H. (2006). Unidirectional development of CD8+ central memory T cells into protective Listeria-specific effector memory T cells. *Eur. J. Immunol.* 36, 1453–1464. <https://doi.org/10.1002/eji.200635874>.
42. Boutet, M., Benet, Z., Guillen, E., Koch, C., M'Homa Soudja, S., Delahaye, F., Fookson, D., and Lauvau, G. (2021). Memory CD8(+) T cells mediate early pathogen-specific protection via localized delivery of chemokines and IFNgamma to clusters of monocytes. *Sci. Adv.* 7, eabf9975. <https://doi.org/10.1126/sciadv.abf9975>.
43. Christo, S.N., Evrard, M., Park, S.L., Gandolfo, L.C., Burn, T.N., Fonseca, R., Newman, D.M., Alexandre, Y.O., Collins, N., Zamudio, N.M., et al. (2021). Discrete tissue microenvironments instruct diversity in resident memory T cell function and plasticity. *Nat. Immunol.* 22, 1140–1151. <https://doi.org/10.1038/s41590-021-01004-1>.
44. Schenkel, J.M., Fraser, K.A., Vezys, V., and Masopust, D. (2013). Sensing and alarm function of resident memory CD8(+) T cells. *Nat. Immunol.* 14, 509–513. <https://doi.org/10.1038/ni.2568>.
45. Li, C., Zhu, B., Son, Y.M., Wang, Z., Jiang, L., Xiang, M., Ye, Z., Beckermann, K.E., Wu, Y., Jenkins, J.W., et al. (2019). The transcription factor Blhhe40 programs mitochondrial regulation of resident CD8(+) T cell fitness and functionality. *Immunity* 51, 491–507.e7. <https://doi.org/10.1016/j.jimmuni.2019.08.013>.
46. Stark, R., Wesselink, T.H., Behr, F.M., Kragten, N.A.M., Arens, R., Koch-Nolte, F., van Gisbergen, K.P.J.M., and van Lier, R.A.W. (2018). TRM maintenance is regulated by tissue damage via P2RX7. *Sci. Immunol.* 3. <https://doi.org/10.1126/sciimmunol.aau1022>.
47. Park, S.L., Buzzai, A., Rautela, J., Hor, J.L., Hochheiser, K., Effern, M., McBain, N., Wagner, T., Edwards, J., McConville, R., et al. (2019). Tissue-resident memory CD8(+) T cells promote melanoma-immune equilibrium in skin. *Nature* 565, 366–371. <https://doi.org/10.1038/s41586-018-0812-9>.
48. Mackay, L.K., Rahimpour, A., Ma, J.Z., Collins, N., Stock, A.T., Hafon, M.L., Vega-Ramos, J., Lauzurica, P., Mueller, S.N., Stefanovic, T., et al. (2013). The developmental pathway for CD103(+)CD8+ tissue-resident memory T cells of skin. *Nat. Immunol.* 14, 1294–1301. <https://doi.org/10.1038/ni.2744>.
49. Kumar, B.V., Ma, W., Miron, M., Granot, T., Guyer, R.S., Carpenter, D.J., Senda, T., Sun, X., Ho, S.H., Lerner, H., et al. (2017). Human tissue-resident memory T cells are defined by core transcriptional and functional signatures in lymphoid and mucosal sites. *Cell Rep.* 20, 2921–2934. <https://doi.org/10.1016/j.celrep.2017.08.078>.
50. Mackay, L.K., Minnich, M., Kragten, N.A., Liao, Y., Nota, B., Seillet, C., Zaid, A., Man, K., Preston, S., Freestone, D., et al. (2016). Hobit and Blimp1 instruct a universal transcriptional program of tissue residency in lymphocytes. *Science* 352, 459–463. <https://doi.org/10.1126/science.aad2035>.
51. Frizzell, H., Fonseca, R., Christo, S.N., Evrard, M., Cruz-Gomez, S., Zanluqui, N.G., von Scheidt, B., Freestone, D., Park, S.L., McWilliam, H.E.G., et al. (2020). Organ-specific isoform selection of fatty acid-binding proteins in tissue-resident lymphocytes. *Sci. Immunol.* 5. <https://doi.org/10.1126/sciimmunol.aaq9283>.

52. Thom, J.T., Weber, T.C., Walton, S.M., Torti, N., and Oxenius, A. (2015). The salivary gland acts as a sink for tissue-resident memory CD8(+) T cells, facilitating protection from local Cytomegalovirus infection. *Cell Rep.* 13, 1125–1136. <https://doi.org/10.1016/j.celrep.2015.09.082>.
53. Bergsbaken, T., and Bevan, M.J. (2015). Proinflammatory microenvironments within the intestine regulate the differentiation of tissue-resident CD8(+) T cells responding to infection. *Nat. Immunol.* 16, 406–414. <https://doi.org/10.1038/ni.3108>.
54. Zhang, N., and Bevan, M.J. (2013). Transforming growth factor-beta signaling controls the formation and maintenance of gut-resident memory T cells by regulating migration and retention. *Immunity* 39, 687–696. <https://doi.org/10.1016/j.immuni.2013.08.019>.
55. Zaid, A., Hor, J.L., Christo, S.N., Groom, J.R., Heath, W.R., Mackay, L.K., and Mueller, S.N. (2017). Chemokine receptor-dependent control of skin tissue-resident memory T cell formation. *J. Immunol.* 199, 2451–2459. <https://doi.org/10.4049/jimmunol.1700571>.
56. Wein, A.N., McMaster, S.R., Takamura, S., Dunbar, P.R., Cartwright, E.K., Hayward, S.L., McManus, D.T., Shimaoka, T., Ueha, S., Tsukui, T., et al. (2019). CXCR6 regulates localization of tissue-resident memory CD8 T cells to the airways. *J. Exp. Med.* 216, 2748–2762. <https://doi.org/10.1084/jem.20181308>.
57. Chatterjee, S., Daenathanasanmak, A., Chakraborty, P., Wyatt, M.W., Dhar, P., Selvam, S.P., Fu, J., Zhang, J., Nguyen, H., Kang, I., et al. (2018). CD38-NAD(+)Axis regulates immunotherapeutic anti-tumor T cell response. *Cell Metab.* 27, 85–100.e8. <https://doi.org/10.1016/j.cmet.2017.10.006>.
58. Bartholin, L., Cyprian, F.S., Vincent, D., Garcia, C.N., Martel, S., Horvat, B., Berthet, C., Goddard-Léon, S., Treilleux, I., Rimokh, R., et al. (2008). Generation of mice with conditionally activated transforming growth factor beta signaling through the TbetaRI/ALK5 receptor. *Genesis* 46, 724–731. <https://doi.org/10.1002/dvg.20425>.
59. Qiu, Z., Khairallah, C., Chu, T.H., Imperato, J.N., Lei, X., Romanov, G., Atakilit, A., Puddington, L., and Sheridan, B.S. (2023). Retinoic acid signaling during priming licenses intestinal CD103+ CD8 TRM cell differentiation. *J. Exp. Med.* 220. <https://doi.org/10.1084/jem.20210923>.
60. Mani, V., Bromley, S.K., Äijö, T., Mora-Buch, R., Carrizosa, E., Warner, R.D., Hamze, M., Sen, D.R., Chasse, A.Y., Lorant, A., et al. (2019). Migratory DCs activate TGF-beta to precondition naive CD8(+) T cells for tissue-resident memory fate. *Science* 366. <https://doi.org/10.1126/science.aav5728>.
61. Milner, J.J., Toma, C., He, Z., Kurd, N.S., Nguyen, Q.P., McDonald, B., Quezada, L., Widjaja, C.E., Witherden, D.A., Crowl, J.T., et al. (2020). Heterogenous populations of tissue-resident CD8(+) T cells are generated in response to infection and malignancy. *Immunity* 52, 808–824.e7. <https://doi.org/10.1016/j.immuni.2020.04.007>.
62. Steinert, E.M., Schenkel, J.M., Fraser, K.A., Beura, L.K., Manlove, L.S., Igýártó, B.Z., Southern, P.J., and Masopust, D. (2015). Quantifying memory CD8 T cells reveals regionalization of immuno surveillance. *Cell* 161, 737–749. <https://doi.org/10.1016/j.cell.2015.03.031>.
63. Chen, Y.G., Chen, J., Osborne, M.A., Chapman, H.D., Besra, G.S., Porcelli, S.A., Leiter, E.H., Wilson, S.B., and Serreze, D.V. (2006). CD38 is required for the peripheral survival of immunotolerogenic CD4+ invariant NK T cells in nonobese diabetic mice. *J. Immunol.* 177, 2939–2947. <https://doi.org/10.4049/jimmunol.177.5.2939>.
64. Kwok, I., Becht, E., Xia, Y., Ng, M., Teh, Y.C., Tan, L., Evrard, M., Li, J.L.Y., Tran, H.T.N., Tan, Y., et al. (2020). Combinatorial single-cell analyses of granulocyte-monocyte progenitor heterogeneity reveals an early unipotent neutrophil progenitor. *Immunity* 53, 303–318.e5. <https://doi.org/10.1016/j.immuni.2020.06.005>.
65. Nakazawa, M. (2023). fmsb: Functions for Medical Statistics Book with some Demographic Data. R package version 0.7.5. <https://CRAN.R-project.org/package=fmsb>.
66. Kolde, R. (2019). pheatmap: Pretty Heatmaps. R package version 1.0.12. <https://CRAN.R-project.org/package=pheatmap>.
67. Melville, J., Lun, A., Djekidel, M.N., Hao, Y., and Eddelbuettel, D. (2022). uwot: The Uniform Manifold Approximation and Projection (UMAP) Method for Dimensionality Reduction. R package version 0.1.14. <https://CRAN.R-project.org/package=uwot>.
68. Kallert, S.M., Darbre, S., Bonilla, W.V., Kreutzfeldt, M., Page, N., Müller, P., Kreuzaler, M., Lu, M., Favre, S., Kreppel, F., et al. (2017). Replicating viral vector platform exploits alarmin signals for potent CD8(+) T cell-mediated tumour immunotherapy. *Nat. Commun.* 8, 15327. <https://doi.org/10.1038/ncomms15327>.
69. van Lint, A., Ayers, M., Brooks, A.G., Coles, R.M., Heath, W.R., and Carbone, F.R. (2004). Herpes simplex virus-specific CD8+ T cells can clear established lytic infections from skin and nerves and can partially limit the early spread of virus after cutaneous inoculation. *J. Immunol.* 172, 392–397. <https://doi.org/10.4049/jimmunol.172.1.392>.
70. Jenkins, M.R., Webby, R., Doherty, P.C., and Turner, S.J. (2006). Addition of a prominent epitope affects influenza A virus-specific CD8+ T cell immunodominance hierarchies when antigen is limiting. *J. Immunol.* 177, 2917–2925. <https://doi.org/10.4049/jimmunol.177.5.2917>.

STAR★METHODS

KEY RESOURCES TABLE

REAGENT or RESOURCE	SOURCE	IDENTIFIER
Antibodies		
Anti-B220 (clone RA3-6B2; BUV395)	BD Biosciences	Cat#563793; RRID: AB_2738427
Anti-B220 (clone RA3-6B2; BV750)	Biolegend	Cat#103261; RRID: AB_2734157
Anti-Bcl2 (clone 3F11; PE)	BD Biosciences	Cat#556537; RRID: AB_396457
Anti-CD8 α (clone 53-6.7; BV711)	BD Biosciences	Cat#563046; RRID: AB_2737972
Anti-CD8 α (clone 53-6.7; BV786)	BD Biosciences	Cat#563332; RRID: AB_2721167
Anti-CD8 α (clone 53-6.7; SparkNIR685)	Biolegend	Cat#100782; RRID: AB_2819775
Anti-CD8 β (clone H35-17.2; BV750)	BD Biosciences	Cat#747505; RRID: AB_2872172
Anti-CD8 β (clone H35-17.2; BV786)	BD Biosciences	Cat#740952; RRID: AB_2740577
Anti-CD11a (clone M17/4; BB700)	BD Biosciences	Cat#742109; RRID: AB_2871382
Anti-CD11b (clone M1/70; BUV661)	BD Biosciences	Cat#612977; RRID: AB_2870249
Anti-CD11c (clone N418; BV605)	Biolegend	Cat#117334; RRID: AB_2562415
Anti-CD11c (clone QA18A72; PE/Fire810)	Biolegend	Cat#161106; RRID: AB_2904307
Anti-CD18 (clone C71/16; BV750)	BD Biosciences	Cat#747153; RRID: AB_2871894
Anti-CD18 (clone M18/2; FITC)	Thermo Fisher Scientific	Cat#11-0181-85; RRID: AB_464960
Anti-CD27(clone LG.3A10; BUV737)	BD Biosciences	Cat#612831; RRID: AB_2739173
Anti-CD27(clone LG.7F9; APC/eF780)	Thermo Fisher Scientific	Cat#47-0271-82; RRID: AB_10853642
Anti-CD31 (clone 390; BV786)	BD Biosciences	Cat#740879; RRID: AB_2740529
Anti-CD38 (clone 90; BV750)	BD Biosciences	Cat#747103; RRID: AB_2871855
Anti-CD38 (clone 90; PE)	Biolegend	Cat#102708; RRID: AB_312929
Anti-CD38 (clone 90; PE/Cy7)	Biolegend	Cat#102718; RRID: AB_2275531
Anti-CD38 (clone 90; APC/Fire810)	Biolegend	Cat#102746; RRID: AB_2890674
Anti-CD39 (clone Y23-1185; BV711)	BD Biosciences	Cat#567295; RRID: AB_2916538
Anti-CD43 (clone 1B11; FITC)	Biolegend	Cat#121206; RRID: AB_493386
Anti-CD43 (clone 1B11; PE/Cy7)	Biolegend	Cat#121218; RRID: AB_528813
Anti-CD43 (clone S11; FITC)	Biolegend	Cat#143204; RRID: AB_10960745
Anti-CD44 (clone IM7; BUV395)	BD Biosciences	Cat#740215; RRID: AB_2739963
Anti-CD44 (clone IM7; BV510)	BD Biosciences	Cat#563114; RRID: AB_2738011
Anti-CD44 (clone IM7; APC/R700)	BD Biosciences	Cat#565480; RRID: AB_2739259
Anti-CD45.1 (clone A20; Biotin)	Biolegend	Cat#110704; RRID: AB_313493
Anti-CD45.1 (clone A20; BV480)	BD Biosciences	Cat#746666; RRID: AB_2743938
Anti-CD45.1 (clone A20; PE/Cy7)	Biolegend	Cat#110730; RRID: AB_1134168
Anti-CD45.1 (clone A20; APC/R700)	BD Biosciences	Cat#565814; RRID: AB_2744397
Anti-CD45.2 (clone 104; APC)	Biolegend	Cat#109814; RRID: AB_389211
Anti-CD45.2 (clone 104; SparkNIR685)	Biolegend	Cat#109864; RRID: AB_2876424
Anti-CD45RB (clone 16A; BUV395)	BD Biosciences	Cat#740211; RRID: AB_2739959
Anti-CD47 (clone miap301; PE)	Biolegend	Cat#127508; RRID: AB_1134117
Anti-CD49a (clone Ha31/8; BV510)	BD Biosciences	Cat#740144; RRID: AB_2739900
Anti-CD49a (clone Ha31/8; BV605)	BD Biosciences	Cat#740375; RRID: AB_2740107
Anti-CD49a (clone Ha31/8; BV711)	BD Biosciences	Cat#564863; RRID: AB_2738987
Anti-CD49a (clone Ha31/8; BB700)	BD Biosciences	Cat#742164; RRID: AB_2861198
Anti-CD49b (clone DX5; FITC)	Biolegend	Cat#108906; RRID: AB_313413
Anti-CD51 (clone RMV-7; PE)	Biolegend	Cat#104106; RRID: AB_2129493
Anti-CD55 (clone RIKO-3; PE)	Biolegend	Cat#131804; RRID: AB_1279265
Anti-CD55 (clone RIKO-3; PE/Cy7)	Biolegend	Cat#131814; RRID: AB_2800634

(Continued on next page)

Continued

REAGENT or RESOURCE	SOURCE	IDENTIFIER
Anti-CD55 (clone RIKO-3; APC)	Biolegend	Cat#131812; RRID: AB_2800632
Anti-CD62L (clone MEL-14; BUV737)	BD Biosciences	Cat#612833; RRID: AB_2870155
Anti-CD62L (clone MEL-14; BV605)	BD Biosciences	Cat#563252; RRID: AB_2738098
Anti-CD62L (clone MEL-14; APC/R700)	BD Biosciences	Cat#565159; RRID: AB_2737397
Anti-CD69 (clone H1.2F3; BV605)	Biolegend	Cat#104530; RRID: AB_2563062
Anti-CD69 (clone H1.2F3; PE/Cy5)	Biolegend	Cat#104510; RRID: AB_313113
Anti-CD69 (clone H1.2F3; SparkNIR685)	Biolegend	Cat#104558; RRID: AB_2876411
Anti-CD73 (clone TY/11.8; BV421)	Biolegend	Cat#127217; RRID: AB_2687251
Anti-CD73 (clone TY/11.8; eF450)	Thermo Fisher Scientific	Cat#48-0731-82; RRID: AB_1272196
Anti-CD73 (clone TY/11.8; BV711)	BD Biosciences	Cat#752736; RRID: AB_2917717
Anti-CD84 (clone mCD84.7; PE)	Biolegend	Cat#122806; RRID: AB_2074756
Anti-CD85k (clone H1.1; PE)	Biolegend	Cat#144904; RRID: AB_2561654
Anti-CD86 (clone PO3; PE)	Biolegend	Cat#105106; RRID: AB_313159
Anti-CD94 (clone 18d3; PE/Cy7)	Biolegend	Cat#105510; RRID: AB_2632679
Anti-CD94 (clone 18d3; APC)	Biolegend	Cat#105512; RRID: AB_2721459
Anti-CD101 (clone Moushi101; PE)	Thermo Fisher Scientific	Cat#12-1011-82; RRID: AB_1210728
Anti-CD101 (clone Moushi101; PE/Cy7)	Thermo Fisher Scientific	Cat#25-1011-82; RRID: AB_2573378
Anti-CD103 (clone 2E7; eF450)	Thermo Fisher Scientific	Cat#48-1031-82; RRID: AB_2574033
Anti-CD103 (clone M290; BV480)	BD Biosciences	Cat#566118; RRID: AB_2739520
Anti-CD122 (clone 5H4; PE)	Biolegend	Cat#105906; RRID: AB_2125736
Anti-CD127 (clone A7R34; BV421)	Biolegend	Cat#135027; RRID: AB_2563103
Anti-CD127 (clone A7R34; PE/eF610)	Thermo Fisher Scientific	Cat#61-1271-82; RRID: AB_2802381
Anti-CD150 (clone TC15-12F12.2; PE)	Biolegend	Cat#115904; RRID: AB_313683
Anti-CD160 (clone 7H1; PE)	Biolegend	Cat#143004; RRID: AB_10960743
Anti-CD205 (clone NLDC-145; PE)	Biolegend	Cat#138214; RRID: AB_10896058
Anti-CD244 (clone m2B4; PE)	Biolegend	Cat#133508; RRID: AB_2072855
Anti-CD244 (clone m2B4; APC)	Biolegend	Cat#133518; RRID: AB_2814027
Anti-CXCR3 (clone CXCR3-173; BV605)	Biolegend	Cat#155915; RRID: AB_2892317
Anti-CXCR3 (clone CXCR3-173; BV650)	Biolegend	Cat#126531; RRID: AB_2563160
Anti-CXCR3 (clone CXCR3-173; FITC)	Biolegend	Cat#126536; RRID: AB_2566565
Anti-CXCR3 (clone CXCR3-173; PE)	Biolegend	Cat#126506; RRID: AB_1027650
Anti-CXCR6 (clone SA051D1; BV421)	Biolegend	Cat#151109; RRID: AB_2616760
Anti-CXCR6 (clone SA051D1; FITC)	Biolegend	Cat#151108; RRID: AB_2572145
Anti-CXCR6 (clone SA051D1; PE)	Biolegend	Cat#151104; RRID: AB_2566546
Anti-CXCR6 (clone SA051D1; PE/ Dazzle594)	Biolegend	Cat#151117; RRID: AB_2721700
Anti-CXCR6 (clone SA051D1; APC)	Biolegend	Cat#151106; RRID: AB_2572143
Anti-CX3CR1 (clone SA011F11; BV421)	Biolegend	Cat#149023; RRID: AB_2565706
Anti-CX3CR1 (clone SA011F11; BV650)	Biolegend	Cat#149033; RRID: AB_2565999
Anti-CX3CR1 (clone SA011F11; BV711)	Biolegend	Cat#149031; RRID: AB_2565939
Anti-CX3CR1 (clone SA011F11; BV785)	Biolegend	Cat#149029; RRID: AB_2565938
Anti-CX3CR1 (clone SA011F11; PE/ Dazzle594)	Biolegend	Cat#149014; RRID: AB_2565698
Anti-CX3CR1 (clone SA011F11; APC)	Biolegend	Cat#149008; RRID: AB_2564492
Anti-CX3CR1 (clone SA011F11; APC/ Fire810)	Biolegend	Cat#149053; RRID: AB_2910300
Anti-DR3 (clone 4C12; PE)	Biolegend	Cat#144406; RRID: AB_2561689
Anti-Eomes (clone Dan11mag; PE/Cy7)	Thermo Fisher Scientific	Cat#25-4875-82; RRID: AB_2573454
Anti-Foxo1 (clone C29H4; AF647)	Cell Signaling	Cat#72874; RRID: AB_2799829

(Continued on next page)

Continued

REAGENT or RESOURCE	SOURCE	IDENTIFIER
Anti-Granzyme A (clone GzA-3G8.5; eF450)	Thermo Fisher Scientific	Cat#48-5831-82; RRID: AB_2574079
Anti-Granzyme B (clone QA16A02; FITC)	Biolegend	Cat#372206; RRID: AB_2687030
Anti-Granzyme B (clone QA16A02; AF700)	Biolegend	Cat#372222; RRID: AB_2728389
Anti-HVEM (clone HMHV-1B18; PE)	Biolegend	Cat#136304; RRID: AB_2203830
Anti-IFN γ (clone XMG1.2; BV480)	BD Biosciences	Cat#566097; RRID: AB_2739501
Anti-IFN γ (clone XMG1.2; FITC)	BD Biosciences	Cat#554411; RRID: AB_395375
Anti-IL-2 (clone JES6-5H4; PE)	Biolegend	Cat#503808; RRID: AB_315302
Anti-IL-2 (clone JES6-5H4; APC)	Biolegend	Cat#503810; RRID: AB_315304
Anti-IL18Ra (clone P3TUNYA; eF450)	Thermo Fisher Scientific	Cat#48-5183-82; RRID: AB_2574069
Anti-IL18Ra (clone P3TUNYA; PE/Cy7)	Thermo Fisher Scientific	Cat#25-5183-82; RRID: AB_2762705
Anti-IL18Ra (clone P3TUNYA; APC)	Thermo Fisher Scientific	Cat#17-7183-42; RRID: AB_2573258
Anti-Integrin β 7 (clone M293; BV650)	BD Biosciences	Cat#743790; RRID: AB_2741758
Anti-Integrin β 7 (clone F1B27; PerCP/Cy5.5)	Biolegend	Cat#121008; RRID: AB_2129312
Anti-Ki67 (clone SolA15; FITC)	Thermo Fisher Scientific	Cat#11-5698-82; RRID: AB_11151330
Anti-Ki67 (clone SolA15; APC/eF780)	Thermo Fisher Scientific	Cat#47-5698-82; RRID: AB_2688065
Anti-KLRG1 (clone 2F1; BV421)	BD Biosciences	Cat#562897; RRID: AB_2737875
Anti-KLRG1 (clone 2F1; BV605)	BD Biosciences	Cat#564013; RRID: AB_2722497
Anti-KLRG1 (clone 2F1; PE/eF610)	Thermo Fisher Scientific	Cat#61-5893-82; RRID: AB_2574630
Anti-KLRG1 (clone 2F1; APC/eF780)	Thermo Fisher Scientific	Cat#47-5893-82; RRID: AB_2573988
Anti-Ly108 (clone 13G3; BV421)	BD Biosciences	Cat#740090; RRID: AB_2739850
Anti-Ly108 (clone 13G3; BV480)	BD Biosciences	Cat#746534; RRID: AB_2743826
Anti-Ly6A/E (clone D7; BUV805)	BD Biosciences	Cat#741916; RRID: AB_2871229
Anti-Ly6D (clone 49-H4; PE)	Biolegend	Cat#138604; RRID: AB_2137349
Anti-Ly6C (clone HK1.4; BV570)	Biolegend	Cat#128030; RRID: AB_2562617
Anti-Ly6C (clone HK1.4; BV605)	Biolegend	Cat#128036; RRID: AB_2562353
Anti-Ly6C (clone HK1.4; BV785)	Biolegend	Cat#128041; RRID: AB_2565852
Anti-MHCII (clone M5/114.15.2; SparkBlue550)	Biolegend	Cat#107662; RRID: AB_2860616
Anti-NK1.1 (clone PK136; BUV563)	BD Biosciences	Cat#741233; RRID: AB_741233
Anti-NK1.1 (clone PK136; BV480)	BD Biosciences	Cat#746265; RRID: AB_2743597
Anti-NK1.1 (clone PK136; SparkNIR685)	Biolegend	Cat#156529; RRID: AB_2910321
Anti-NKG2D (clone CX5; APC)	Thermo Fisher Scientific	Cat#130212; RRID: AB_1236372
Anti-PD1 (clone 29F.1A12; BV711)	Biolegend	Cat#135231; RRID: AB_2566158
Anti-PD1 (clone 29F.1A12; BV785)	Biolegend	Cat#329930; RRID: AB_2563443
Anti-PD1 (clone 29F.1A12; PE/Fire810)	Biolegend	Cat#135253; RRID: AB_2910293
Anti-Runx3 (clone R3-5G4; PE)	BD Biosciences	Cat#564814; RRID: AB_2738969
Anti-Tbet (clone 4B10; BV421)	Biolegend	Cat#644815; RRID: AB_10896427
Anti-Tbet (clone 4B10; AF488)	Biolegend	Cat#644830; RRID: AB_2566019
Anti-Tbet (clone 4B10; PE)	Biolegend	Cat#644810; RRID: AB_2200542
Anti-TCF1 (clone C63D9; AF488)	Cell Signaling	Cat#2203S; RRID: AB_2199302
Anti-TCR β (clone H57-597; BV650)	Biolegend	Cat#109251; RRID: AB_2810348
Anti-TCR β (clone H57-597; BV711)	Biolegend	Cat#109243; RRID: AB_2629564
Anti-TCR β (clone H57-597; APC/Fire750)	Biolegend	Cat#109246; RRID: AB_2629697
Anti-TCR γ δ (clone GL3; BV605)	Biolegend	Cat#118129; RRID: AB_2563356
Anti-TCR γ δ (clone GL3; PerCP/eF710)	Thermo Fisher Scientific	Cat#46-5711-82; RRID: AB_2016707
Anti-Thy1.1 (clone OX-7; Biotin)	Biolegend	Cat#202510; RRID: AB_2201417
Anti-Thy1.1 (clone OX-7; AF488)	Biolegend	Cat#202506; RRID: AB_492882
Anti-Thy1.1 (clone OX-7; PerCP)	Biolegend	Cat#202512; RRID: AB_1595487
Anti-Thy1.1 (clone OX-7; AF700)	Biolegend	Cat#202528; RRID: AB_1626241
Anti-Thy1.2 (clone 53-2.1; BUV395)	BD Biosciences	Cat#565257; RRID: AB_2739136

(Continued on next page)

Continued

REAGENT or RESOURCE	SOURCE	IDENTIFIER
Anti-Thy1.2 (clone 53-2.1; PerCP)	Biolegend	Cat#140316; RRID: AB_10642813
Anti-TNF (clone MP6-XT22; BV711)	Biolegend	Cat#506349; RRID: AB_2629800
Anti-V α 2 (clone B20.1; BUV615)	BD Biosciences	Cat#751416; RRID: AB_2875415
Anti-V α 2 (clone B20.1; BV421)	BD Biosciences	Cat#562944; RRID: AB_2737910
Anti-V α 2 (clone B20.1; BV480)	BD Biosciences	Cat#746615; RRID: AB_2743895
Anti-V α 2 (clone B20.1; PE)	BD Biosciences	Cat#553289; RRID: AB_394760
Anti-V α 2 (clone B20.1; PE/Cy7)	BD Biosciences	Cat#560624; RRID: AB_1727584
Anti-Ter119 (clone Ter119; purified from hybridoma)	In house	N/A
MHCII (clone M5/114.15.2 purified from hybridoma)	In house	N/A
CD4 (clone GK1.5; purified from hybridoma)	In house	N/A
CD11b (clone: M1/70; purified from hybridoma)	In house	N/A
F4/80 (clone BM8; purified from hybridoma)	In house	N/A
Anti-Thy1 (clone T24; purified from hybridoma)	In house	N/A
Anti-CD3 (clone 145-2C11)	BioXCell	Cat#BE0001-1; RRID: AB_1107634
Anti-CD28 (clone 37.51)	BioXCell	Cat#BE0015-1; RRID: AB_1107624
Anti-Gr1 (clone NIMP-R14)	BioXCell	Cat#BE0075; RRID: AB_10312146
Anti-ARTC2 (Treg protector) (clone S+16a)	Biolegend	Cat#149802; RRID: AB_2565494
Bacterial and virus strains		
Herpes simplex virus (HSV-OVA)	D. Tscharke, Australian National University	N/A
Influenza virus A/HKX31 (X31-OVA)	P. Doherty, University of Melbourne	N/A
Lymphocytic choriomeningitis virus (LCMV) Armstrong strain	R. Ahmed, Emory University	N/A
Lymphocytic choriomeningitis virus (LCMV)-OVA	D. Merkler, University of Geneva	N/A
<i>Listeria monocytogenes</i> (Lm-OVA), InlA mutant	L. Lefrancois, University of Connecticut	N/A
Recombinant adeno-associated virus (rAAV-OVA)	P. Bertolino, Centenary Institute	N/A
Vaccinia virus (VV-OVA)	D. Tscharke, Australian National University	N/A
Chemicals, peptides, and recombinant proteins		
H-2D(b) LCMV GP33 biotinylated monomer (KAVYNFATM)	NIH tetramer core facility	N/A
H-2D(b) LCMV NP396 biotinylated monomer (FQPQNGQFI)	NIH tetramer core facility	N/A
GP33 peptide (KAVYNFATM)	Auspep	N/A
Alt-R S.p. Cas9 Nuclease V3	Integrated DNA Technologies	Cat#1081059
Collagenase type III	Worthington Biochemical	Cat#LS004183
Liberase TL Research Grade	Sigma-Aldrich	Cat#5401020001
Deoxyribonuclease I from bovine pancreas	Sigma-Aldrich	Cat#DN25
Percoll	Thermo Fisher Scientific	Cat#GE17-0891-01
1,4-Dithioerythritol	Sigma-Aldrich	Cat#D8255
10X HBSS, no Ca ²⁺ , no Mg ²⁺	Thermo Fisher Scientific	Cat#14180046

(Continued on next page)

Continued

REAGENT or RESOURCE	SOURCE	IDENTIFIER
eBioscience 1X RBC Lysis Buffer	Thermo Fisher Scientific	Cat#00-4333-57
Brefeldin A from Penicillium	Sigma-Aldrich	Cat#B6542
β-Nicotinamide adenine dinucleotide sodium salt (NAD)	Sigma-Aldrich	Cat#N0632
Human recombinant IL-2	Peptech	Cat#200-02
EDTA	Sigma-Aldrich	Cat#E5134
Trypsin-EDTA Solution 10X	Sigma-Aldrich	Cat#59418C
LPS from <i>E.coli</i> O111:B4	Sigma-Aldrich	Cat#L4391
Bovine serum albumin	Sigma-Aldrich	Cat#A7906
Fetal Bovine serum	Sigma-Aldrich	Cat#12007C
Penicillin/Streptomycin	Sigma-Aldrich	Cat#P0781
2-Mercaptoethanol	Sigma-Aldrich	Cat#M3148
L-Glutamine	Sigma-Aldrich	Cat# G8540
DMEM	In house	N/A
RPMI	In house	N/A
HEPES	Sigma-Aldrich	Cat#H3375
BioMag Goat Anti-Rat IgG	Qiagen	Cat#310107
Sphero blank calibration particles	BD Bioscience	Cat#556296
Pierce 16% Formaldehyde (w/v), Methanol-free	Thermo Fisher Scientific	Cat#28908
DAPI (4',6-Diamidino-2-Phenylindole, Dilactate)	Biolegend	Cat#422801
Critical commercial assays		
LEGENDScreen mouse	Biolegend	Cat#700009
Zombie Yellow Fixable Viability Kit	Biolegend	Cat#423104
Zombie NIR Fixable Viability Kit	Biolegend	Cat#423106
RNeasy Plus Micro Kit	Qiagen	Cat#74034
High-Capacity cDNA Reverse Transcription Kit	Thermo Fisher Scientific	Cat#4368813
TaqMan PreAmp Master Mix	Thermo Fisher Scientific	Cat#488593
TaqMan Fast Advanced Master Mix	Thermo Fisher Scientific	Cat#4444557
P3 Primary Cell 4D-NucleofectorTM X Kit S	Lonza	Cat#V4XP-3032
BD Cytofix/Cytoperm Fixation/Permeabilization Kit	BD Bioscience	Cat#554714; RRID: AB_2869008
eBioscience FoxP3/Transcription Factor Staining Buffer Set	Thermo Fisher Scientific	Cat#00-5523-00
Deposited data		
Infinityflow dataset #1: P14 memory CD8 ⁺ T cells across 6 tissues (LCMV-Arm 60 d p.i.)	This paper	http://mackaylab.mdhs.unimelb.edu.au/InfinityFlow1/
Infinityflow dataset #2: P14 spleen T _{CIRCM} cells (LCMV-Arm 60 d p.i.)	This paper	http://mackaylab.mdhs.unimelb.edu.au/InfinityFlow2/
Infinityflow dataset #3: OT-I spleen T _{CIRCM} cells (LCMV-OVA and X31-OVA, 20 d and 100 d p.i.)	This paper	http://mackaylab.mdhs.unimelb.edu.au/InfinityFlow3/
Infinityflow dataset #3: OT-I memory CD8 ⁺ T cells across 7 tissues (LCMV-OVA, Lm-OVA, HSV-OVA and X31-OVA, 50 d p.i.)	This paper	http://mackaylab.mdhs.unimelb.edu.au/InfinityFlow4/
Experimental models: Cell lines		
Platinum-E (Plat-E) cell line	Cell Biolabs, Inc.	Cat#RV-101; RRID: CVCL_B488
Experimental models: Organisms/strains		
Mouse: C57BL/6J	The Jackson Laboratory	Strain #:000664; RRID: IMSR_JAX:000664
Mouse: B6;D2-Tg(TcrLCMV)327Sdz/JDvsJ (P14)	The Jackson Laboratory	Strain #:004694; RRID:IMSR_JAX:004694
Mouse: C57BL/6-Tg(TcraTcrb)1100Mjb/J (OT-I)	The Jackson Laboratory	Strain #:003831; RRID:IMSR_JAX:003831

(Continued on next page)

Continued

REAGENT or RESOURCE	SOURCE	IDENTIFIER
Mouse: B6.SJL- <i>Ptprc</i> ^a <i>Pepc</i> ^b /BoyJ (CD45.1)	The Jackson Laboratory	Strain #:002014; RRID:IMSR_JAX:002014
Mouse: B6.PL- <i>Thy1</i> ^a /CyJ (Thy1.1)	The Jackson Laboratory	Strain #:000406; RRID:IMSR_JAX:000406
Mouse: B6;129- <i>Tgfb2</i> ^{tm1Karl} /J (<i>Tgfb2</i> ^{f/f})	The Jackson Laboratory	Strain #:012603; RRID:IMSR_JAX:012603
Mouse: B6.Cg-Tg(Lck-cre)3779Nik/J (dLck ^{cre})	The Jackson Laboratory	Strain #:012837; RRID:IMSR_JAX:012837
Mouse: Zfp683-TdTomato (Hobit ^{Tom})	N/A	N/A
Mouse: B6.129P2-Cxcr6 ^{tm1Litt} /J (Cxcr6 ^{-/-})	The Jackson Laboratory	Strain #:005693; RRID:IMSR_JAX:005693
Oligonucleotides		
<i>Sirt1</i> sgRNA#1: GAUUCUGCAACCUGCUCCA	Synthego	N/A
<i>Sirt1</i> sgRNA#2: GGTCTGGGAAGTCCACCGCA	Synthego	N/A
<i>Cd19</i> sgRNA: AAUGUCUCAGACCAUAUGGG	Synthego	N/A
<i>Sirt1</i> TaqMan probe	Thermo Fisher Scientific	Mm01168521_m1
<i>Hprt</i> TaqMan probe	Thermo Fisher Scientific	Mm00446968_m1
<i>Tbp</i> TaqMan probe	Thermo Fisher Scientific	Mm00446973_m1
Recombinant DNA		
pCL-Eco retrovirus packaging vector	Addgene	RRID: Addgene_12371
pMIG II vector	Addgene	RRID: Addgene_52107
pMIG II TGFBI-CA vector	This paper	N/A
pLMPd-Ametrine	Transomic	shRNA retroviral target gene set
shERWOOD UltramiR Retroviral shRNA target gene set for gene CD38	Transomic	Cat#TRMSU2000-12494
Software and algorithms		
FlowJo v10	Tree Star	https://www.flowjo.com/
Prism v9	GraphPad	https://www.graphpad.com/
OMIQ	Dotmatics	https://www.omiq.ai/
InfinityFlow v1.8.0	Becht, 2020 ²⁷	https://bioconductor.org/packages/infinityFlow/
oneSENSE v1.20	Chen, 2022 ³⁴	https://bioconductor.org/packages/oneSENSE/
fmsb v0.7.5 (Radar plot)	Nakazawa, 2023 ⁶⁵	https://cran.r-project.org/package=fmsb
pheatmap v1.0.12	Kolde, 2019 ⁶⁶	https://cran.r-project.org/package=pheatmap
uwot v0.1.14	Melville, 2022 ⁶⁷	https://cran.r-project.org/package=uwot

RESOURCE AVAILABILITY**Lead contact**

Further information and requests for resources and reagents should be directed to and will be fulfilled by Laura Mackay (lkmacay@unimelb.edu.au) upon reasonable request.

Materials availability

Plasmids generated in this study are available from the [lead contact](#) upon request.

Data and code availability

InfinityFlow datasets are publicly available: <http://mackaylab.mdhs.unimelb.edu.au/InfinityFlow/>

This paper does not report original code.

Any additional information required to reanalyse the data reported in this paper is available from the [lead contact](#) upon request.

EXPERIMENTAL MODEL AND SUBJECT DETAILS

Mice

C57BL/6, B6.SJL-PtprcaPep3b/BoyJ (CD45.1), B6.SJL-PtprcaPep3b/BoyJ × C57BL/6 (CD45.1×CD45.2), P14 CD45.1, P14 Thy1.1, OT-I CD45.1, OT-I *Tgfb2^{fl/fl}*.dLck-cre CD45.1 (OT-I *Tgfb2^{-/-}*), B6.129P2-Cxcr6tm1Litt/J (termed *Cxcr6^{-/-}*) mice were bred in the Department of Microbiology and Immunology. *Zfp683^{taTomato/+}* (termed *Hobit^{Tom}*) were generated by the Kallies lab and will be described in detail elsewhere. Female mice were used for experiments at 6–20 weeks of age. All animal experiments were approved by the University of Melbourne Animal Ethics Committee. P14 mice express a transgenic T cell receptor recognizing the LCMV glycoprotein-derived epitope GP_{33–41}. OT-I mice express a transgenic T cell receptor recognizing the ovalbumin epitope OVA_{257–264}. Bone marrow chimeric mice were generated by irradiation of CD45.1 mice (550 rad 3 h apart, × 2) followed by reconstitution with 2 × 10⁶ congenically distinct WT (CD45.1⁺CD45.2⁺) and *Cxcr6^{-/-}* (CD45.2⁺) donor bone marrow cells. Residual T cells were depleted the next day using 100 µg of anti-Thy1 (T24) antibody i.p. and mice were rested for 8 weeks following reconstitution.

METHOD DETAILS

T cell transfer

Adoptive transfers of naive P14 or OT-I T cells were carried out intravenously (i.v.) with lymph node suspensions. Naive P14 or OT-I T cells were transferred at a total number of 5 × 10⁴ or 2.5 × 10⁴ cells/population in co-transfer experiments, where cell types were transferred at a ratio of 1:1.

Infections

LCMV-OVA (artLCMV) was obtained from Doron Merkler.⁶⁸ LCMV infection was performed by intraperitoneal (i.p.) injection of 2 × 10⁵ pfu of the Armstrong strain of LCMV or 10⁵ pfu of the OVA strain of LCMV. Lm infection was performed through oral feeding using a recombinant strain that carries OVA and a mutated internalin A. Briefly, individually housed mice were deprived of food, water and enrichment for 5 h before being fed a 1 cm³ piece of bread inoculated with 10⁹ cfu of Lm-OVA in PBS as described.⁴³ HSV infection was performed by scarification as described,⁶⁹ using 10⁶ pfu of the KOS strain of the virus modified to express OVA. Influenza infection was performed by intranasal (i.n.) administration of 10⁴ pfu of the A/HKX31 (H3N2) strain of the virus modified to express OVA as described.⁷⁰ In some experiments, mice that were previously infected with LCMV-OVA were challenged with i.v. administration of VV-OVA (1–5 × 10⁶ pfu), or rAAV-OVA (10⁹ viral genome copies).

In vivo treatments

To modulate numbers of T_{CIRCM} or T_{RM} cells, mice were treated with anti-Gr1 antibody (NIMP-R14; BioXCell) or NAD⁺ (Sigma-Aldrich) where indicated. To deplete T_{CIRCM}, mice received 200 µg of anti-Gr1 antibody or PBS and were analysed 7 days later. To induce the depletion of T_{RM} via P2RX7 activation, mice received 60 mg of NAD⁺ (pH=7) or PBS and were analysed 1 day later.

Mouse tissue processing

Mice were i.v. injected with 4 µg of biotin-conjugated anti-CD8β (YTS156.7.7) 4 min before euthanasia where indicated. Blood was collected via an incision in the submandibular region and was then lysed using 1X RBC lysis buffer (eBioscience). Spleen and lymph nodes were processed into a single-cell suspension using metal meshes. Femurs were flushed using a 23-gauge syringe filled with 1X PBS to obtain BM single-cell suspension. Livers were meshed through 70 µm cell strainers and pellets were resuspended in 35% isotonic Percoll (GE Healthcare) prior to density gradient centrifugation (500g, 20 min). BM, spleen and liver red blood cells were lysed using 1X RBC lysis buffer (eBioscience). Small intestine was cleared of luminal contents and Peyer's patches were excised. Intestines were longitudinally opened, cut into ~1 cm fragments which were incubated at 37°C for 30 min with lateral rotation (230 rpm) in 10% Hanks' balanced salt solution/HEPES containing dithioerythritol (0.15 mg/mL; Sigma Aldrich). Intra-epithelial lymphocytes were then purified using a 44/70% Percoll gradient centrifugation. FRT, kidneys, lungs and SG were collected in Collagenase III (3 mg/mL) and DNase I (5 µg/mL; Roche), chopped into fine pieces and incubated for 45 min at 37°C. Digested pieces were homogenised, passed through a 70 µm cells strainer, and lymphocytes were purified using a 44/70% Percoll gradient centrifugation. Flank skin was shaved and depilated and an area of 1–3 cm² was excised. Skin was incubated in Liberase TL Research Grade solution (0.25 mg/mL; Sigma Aldrich) and DNase I (5 µg/mL; Roche) at 37°C for 30 min and the epidermis separated from the dermis before finely chopping and incubation for a further 60 min at 37°C. Digested skin was homogenised into a single-cell suspension and sequentially passed through 70 µm and 30 µm nylon mesh.

Flow cytometry

Mouse cells were stained at 4°C for 60 min with the following antibodies (all purchased from BD Bioscience, Biolegend or ThermoFisher): anti-B220 (RA3-6B2), anti-CD8α (53-6.7), anti-CD8β (H35-17.2), anti-CD11a (M17/4), anti-CD11b (M1/70), anti-CD11c (N418), anti-CD18 (C71/16 or M18/2), anti-CD27 (LG.7F9), anti-CD31 (390), anti-CD38 (90), anti-CD39 (Y23-1185), anti-CD43 (1B11 or S11), anti-CD44 (IM7), anti-CD45.1 (A20), anti-CD45.2 (104), anti-CD45RB (16A), anti-CD47 (miap301), anti-CD49a (Ha31/8), anti-CD49b (DX5),

anti-CD51 (RMV-7), anti-CD55 (RIKO-3), anti-CD62L (MEL-14), anti-CD69 (H1.2F3), anti-CD73 (TY11.8), anti-CD84 (mCD84.7), anti-CD85k (H1.1), CD86 (PO3), anti-CD94 (18d3), anti-CD101 (Moushi101), anti-CD103 (2E7 or M290), anti-CD122 (5H4), anti-CD127 (A7R34), anti-CD150 (TC15-12F12.2), anti-CD160 (7H1), anti-CD205 (NLDC-145), anti-CD244 (m2B4), anti-CXCR3 (CXCR3-173), anti-CXCR6 (SA051D1), anti-CX3CR1 (SA011F11), anti-DR3 (4C12), anti-HVEM (HMHV-1B18), anti-IL-18Ra (P3TUNYA), anti-IntegrinB7 (FIB27 or M293), anti-KLRG1 (2F1), anti-Ly108 (13G3), anti-Ly6A/E (D7), anti-Ly6D (49-H4), anti-Ly6C (HK1.4), anti-MHCII (M5/114.15.2), anti-NK1.1 (PK136), anti-NKG2D (CX5), anti-PD-1 (29F.1A12), anti-TCR β (H57-597), anti-TCR $\gamma\delta$ (GL3), anti-Thy1.1 (OX-7), anti-Thy1.2 (53-2.1), anti-V α 2 (B20.1). For TF staining, cells were fixed and permeabilized using FoxP3 Transcription Factor staining buffer set and stained with the following antibodies (all purchased from BD, Biolegend, Cell Signaling or ThermoFisher): anti-Bcl2 (3F11), anti-Eomes (Dan11mag), anti-Foxo1 (C29H4), anti-Ki67 (SolA15), anti-Runx3 (R3-5G4), anti-Tbet (4B10) and anti-TCF1 (C63D9). Dead cells were excluded from analysis using DAPI (0.5 μ M; Biolegend), Zombie Yellow or Zombie NIR fixable live/dead (Biolegend). For flow cytometry experiments, samples were acquired on a 5-laser BD LSRLFortessa (BD Biosciences) or a 5-laser Cytek Aurora. For cell sorting experiments, memory T cells from the spleen (CD8 α^+ V α 2 $^+$ CD45.1 $^+$) were sorted according to the gating strategy described in [Figure 1I](#) using a 5-laser BD FACSAria III (BD Bioscience) or a 4-laser Beckman Coulter Cytoflex SRT (>95% purity). Data was analysed on Flowjo v10 (Treestar) or OMIQ (<https://www.omiq.ai/>).

LEGENDScreen and InfinityFlow analysis

To generate the LCMV GP33-specific memory T cells dataset across tissues, C57BL/6 mice were i.v. transferred with 5×10^4 P14 Thy1.1 T cells and were infected with LCMV 1 day later (n=20 mice). After 60 days, spleen, BM (2 femurs and 2 tibias), liver, kidneys, SG and SI-IEL were processed into single cell suspension as described above. Alternatively, mice were transferred with OT-I CD45.1 T cells and were infected with LCMV-OVA, Lm-OVA, HSV-OVA or X31-OVA 1 day later. To generate the OVA-specific T_{CIRCM} dataset, LCMV-OVA and X31-OVA infected mice were sacrificed 20 dpi or 100 dpi and OT-I T cells were isolated from the spleen (n=5 mice per infection and per timepoint). To generate the OVA-specific memory T cells dataset across tissues, LCMV-OVA, Lm-OVA, HSV-OVA or X31-OVA were sacrificed 50 dpi. OT-I T cells were isolated from the following organs: spleen, liver, FRT, SG and SI-IEL for LCMV-OVA infected mice (n=5 mice); spleen, liver, SG and SI-IEL for Lm-OVA infected mice (n=5 mice); spleen and skin (both flanks) for HSV-OVA (n=10 mice); spleen and lung (n=5 mice). For all datasets, CD8 $^+$ T cells were enriched from tissue suspensions with the exception of FRT, SI-IEL and skin, by staining with a homemade antibody cocktail (rat anti-CD4 (GK1.5), anti-CD11b (M1/70), anti-F4/80 (Cl:A3-1), anti-erythrocyte (Ter119) and anti-I-A/I-E (M5/114.15.2)) and then incubating with goat anti-rat IgG-coupled magnetic beads (Qiagen) before removing bead-bound cells. 1:3 of the enriched spleen suspension was used for downstream analysis while other organs were kept undiluted. Enriched suspensions from each tissue were stained with anti-Thy1.1 and were barcoded using distinct streptavidin combinations before being pooled together (see [Figure S1A](#)). Cells were counted, resuspended at 20×10^6 cells/mL and stained in FACS buffer (PBS + 5% BSA + 0.5mM EDTA) with anti-CD16/32 (2.4G2) and live/dead NIR for 20 min at 4°C. Cells were washed, resuspended at 20×10^6 cells/mL and stained with backbone antibody panel for 60 min at 4°C (see [Figure 1A](#)). Cells were washed, resuspended at 4×10^6 /mL, aliquoted in each well of the LEGENDScreen Mouse PE Kit (Biolegend) (LCMV GP33-specific memory T cells dataset across tissues and OVA-specific T_{CIRCM} dataset) and stained for 45 min at 4°C according to manufacturer instructions ([Table S2](#)). Alternatively, to generate the OVA-specific memory T cells dataset across tissues, cells were aliquoted in individual wells containing a selection of PE-conjugated markers ([Table S5](#)). Cells were washed, fixed using Biolegend fixation buffer, resuspended in 100 μ L per well and acquired on a 5-laser BD LSRLFortessa (BD Bioscience) (LCMV GP33-specific dataset) or a 5-laser Aurora (Cytek) (all OVA-specific datasets). Following data collection, FCS files were individually examined in FlowJo (Tree Star) for compensation adjustment and quality control. Doublets and dead cells were excluded from analysis, and cells with lymphocytic morphology were exported into new FCS files for each well which were used as input for InfinityFlow prediction pipeline using the *infinityFlow* R package.²⁷ More specifically, each channel from the input data excluding FSC-A, SSC-A, Live-Dead and streptavidin-barcodes was scaled using logicle transformation with parameters estimated with the *infinityFlow* R package. For each well, 50% of the data was randomly selected and to train XGBoost non-linear regression model implemented in the *xgboost* R package with a depth of 500 trees, a learning rate of 0.05 and otherwise default parameters. This model aimed at predicting the intensity of the PE-conjugated variable antibody expression from the backbone expression data for each cell in the well. From non-training data, up to 30,000 events were randomly selected for each well and concatenated across wells to generate the backbone matrix of the InfinityFlow output. Predictions from all models were generated across all of these non-training events to generate the final InfinityFlow matrix, containing backbone-measured and variable-predicted expression intensities. These predictions were finally concatenated and dimensionally reduced with UMAP on backbone parameters to generate a single data matrix (>200 dimensions), using the *uwot* R package with parameters n_neighbors = 15, min_dist = 0.2, metric = "euclidean" and n_epochs = 2000. For downstream analysis, P14 or OT-I T cells were debarcoded according to tissue of origin.

Dimensionality reduction, correlation and trajectory inference

InfinityFlow augmented data matrix was scaled using hyperbolic arcsine (asinh) transformation with OMIQ cloud platform (<https://www.omiq.ai/>). UMAP dimensionality reduction was performed in R using the *uwot* R package or with OMIQ. PCA analysis was carried out in Prism 9 (Treestar). One-SENSE analysis was performed in R as described,³⁴ with the exception that UMAP dimensionality reduction was used instead of t-SNE. UMAP and one-SENSE plots were colour coded using the *ggplot2* R package. Wanderlust

trajectory inference was carried out using OMIQ with default parameters using CD62L^{hi} events as starting point. Heatmaps and correlation were generated using asinh transformed median expression in R using the *pheatmap* R package. Stain indexes were calculated using the *StainIndex* Flowjo plugin.

Generation of murine BM-derived DCs

BM cells were RBC lysed using ACK and cultured in complete RPMI (supplemented with 10% FCS, Penicillin (50U/mL), Streptomycin (100µg/mL), L-glutamine (2mM), 2-mercaptoethanol (50µM) and HEPES (5mM)) in the presence of Flt3L (200ng/mL; Peprotech) and GM-CSF (80ng/mL; Peprotech). On day 3, half of the medium was replaced with fresh RPMI supplemented with GM-CSF (80ng/mL). On day 7, DCs were activated overnight with LPS (150ng/mL; Sigma-Aldrich). On day 8, DCs were pulsed with GP33 peptide (KAVYNFATM; 1µg/mL) for 45min. For DC-GP33 *in vivo* reactivation assays, 2.5×10^6 peptide-pulsed DCs were i.v. transferred into mice, which were sacrificed 6h later.

T cells stimulations and cytokine staining

For the quantification of CD69 expression, spleen single cell suspensions were cultured in complete RPMI in the presence of IL-33 (Peprotech; 500ng/mL), TNF α (Peprotech; 625ng/mL), type I IFN (R&D; 5000U/mL) or anti-CD3 (BioXCell; 5µg/mL) for 6h at 37°C. For the assessment of cytokine production *in vitro*, spleen single cell suspensions were cultured in complete RPMI in the presence of GP33 peptide (KAVYNFATM; 10ng/mL), brefeldin A (10 µg/mL; Sigma-Aldrich) and anti-CD107a (1D4B, Biolegend) for 4h at 37°C. For GP33 peptide *in vivo* rechallenge assays, mice were treated with 5µg of peptide i.v. and were sacrificed 2h later. For VV-OVA rechallenge assays, mice were treated with 50µg of anti-ARTC2 nanobody i.v. (s+16a, Biolegend) prior to tissue harvest. Single cell suspensions of indicated tissues were cultured in the presence of brefeldin A for 3h at 37°C. For intracellular staining, cells were processed using BD fixation and permeabilization kit and stained with the following antibodies (all purchased from BD, Biolegend, or ThermoFisher): GranzymeA (GzA-3G8.5), Granzyme B (QA16A02), IL-2 (JES6-5H4), IFN γ (XMG1.2) and TNF α (MP6-XT22).

CRISPR/Cas9 gene editing of CD8 $^+$ T cells

sgRNA targeting *Sirt1* (5'-GAUCCUGCAACCUGCUCCA-3' and 5'- GGTCTGGGAAGTCCACCGCA-3'), or scramble control (5'-GCACUACCAGAGCUAACUCA-3') were purchased from Synthego (CRISPRRevolution sgRNA EZ Kit). sgRNA/Cas9 RNP were formed by incubating 1µL of sgRNA (0.3nmol/µL) with 0.6µL Alt-R S.p. Cas9 Nuclease V3 (10mg/mL; Integrated DNA Technologies) for 10min at room temperature. *In vitro* activated (anti-CD3 and anti-CD28, 5 µg/mL each for 48 h) P14 T cells were resuspended in 20µL P3 buffer (P3 primary cell 4D-Nucleofector X Kit S; Lonza), mixed with sgRNA/Cas9 RNP and electroporated using Lonza 4D-Nucleofector system (pulse code: CM137). Cells were further expanded for 3 d in the presence of IL-2 (25U/mL; Peprotech). 1×10^5 P14 T cells edited with control (*sgCtrl*) and *Sirt1* (*sgSirt1*) guides were mixed at 1:1 ratio and were transferred i.v. into wild-type recipients, and were infected with LCMV.

qPCR

RNA was extracted from sorted samples using RNeasy Plus Micro Kit (QIAGEN) according to the manufacturer's instructions. mRNA was converted into cDNA using High Capacity cDNA Reverse Transcription Kit, and genes of interest were preamplified using TaqMan PreAmp Master Mix (ThermoFisher Scientific). Gene expression was analysed by real-time PCR using the StepOnePlus Real-Time PCR System (ThermoFisher Scientific), TaqMan Fast Advanced Master Mix, and the following TaqMan probes (all from Thermo Fisher Scientific): Hprt Mm00446968_m1, Sirt1 Mm01168521_m1, Tbp Mm00446973_m1. Cycle-threshold values were determined for genes individually, and gene expression was normalized according to the $2^{-\Delta Ct}$ method to the housekeeping gene Hprt or Tbp.

Retroviral transduction of CD8 $^+$ T cells

Retroviruses were produced using Plat-E cells (Cell Biolabs) which were transfected with pCL-Eco, pMSCV-IRES-GFP II (pMIG II) and pLMPd-Ametrine based vectors. Plat-E cells were seeded in 96-mm dishes at a density of 7×10^6 cells 12 hours before transfection with 14µg of pLMPd-Ametrine and 7µg of pCL-Eco plasmid DNA using the CalPhos Mammalian Transfection kit (Takara). Viral supernatants were harvested 48 hours later and filtered (0.45µm; Millipore). CD38 shRNAmir vector was purchased from Transomics. A truncated version of TGF-βRI (TGF-βRI/CA)⁵⁸ cDNA was cloned into pMIG II vector. Purified naïve P14 CD8 $^+$ T cells were *in vitro* activated with anti-CD3 (145-2C11) and anti-CD28 (37.51) (5µg/mL for each; both from BioXCell) for 24 hours and were "spinfecte" with 0.5mL of retroviral supernatant in 24-well plates coated with Retronectin (32µg/mL; Takara). CD8 $^+$ T cells were further expanded for 3 days in the presence of IL-2 (25U/mL; Peprotech). Transduction efficiency was determined by Ametrine or GFP expression. Cells transduced with a CD19 (*shCtrl*) or CD38 (*shCd38*) shRNAmirs or were co-transduced with EV-GFP or TGF-βRI/CA-GFP retroviruses, and were mixed at 1:1 ratio. 2×10^5 transduced cells of the relevant specificity were administered intravenously in mice that were infected with LCMV Armstrong one day before.

QUANTIFICATION AND STATISTICAL ANALYSIS

Statistics analyses were calculated by performing unpaired t-test, One-way ANOVA test with Tukey's post-test or Two-way ANOVA test with Sidak's post-test using Prism 9 (GraphPad). *p < 0.05, **p < 0.01, ***p < 0.001, and ****p < 0.0001.